NTNU

Norwegian University of
Science and Technology

A Finite-Size Study on Samarium-Substituted Bismuth Ferrite
Multiferroic and Lead-Free Piezoelectric Materials

Dag Håkon Haneberg

Nanotechnology

Submission date: June 2011
Supervisor: Tor Grande, IMTE
Co-supervisor: Sverre Selbach, IMT

Norwegian University of Science and Technology
Department of Materials Science and Engineering

A Finite-Size Study on
Samarium-Substituted Bismuth Ferrite
Multiferroic and Lead-Free Piezoelectric Materials

June 15, 2011

Dag H. Haneberg

.

Declaration

I hereby declare that the work in this project has been performed independently and in accordance with the examination regulations of Norwegian University of Science and Technology (NTNU).

_____
Dag Håkon Haneberg

.

Abstract

Multiferroic materials combine two or more ferroic orders such as ferroelectricity, ferromagnetism and ferroelasticity. They have a great interest for the development of the next generations of digital electronic memory devices. Bismuth ferrite has shown to posess both ferroelectric and magnetic order at room temperature, which makes it both scientifically and comercially interesting.

The negative impact on the environment by using lead in mass-produced units has made development of lead-free piezoelectric materials for use in sensors, actuators and transducers prioritized and samarium substituted bismuth ferrite has shown to posess a piezoelectric response high enough to be considered for commercial applications.

In this project work, 10mol% samarium substituted bismuth ferrite, $Bi_{0.9}Sm_{0.1}FeO_3$, powders have been synthesized using a wet-chemical method and calcined to a range of temperatures to achieve a range of nanocrystalline sizes in the powders. These powders has been investigated using X-ray diffraction (XRD), Rietveld refinement and differential scanning calorimetry (DSC). The powders have also been milled, pressed and sintered to pellets for ferroelectric and piezoelectric testing.

The crystal structure was found to belong to the R3c group as for bismuth ferrite, $BiFeO_3$, but the unit cell geometry is changed slightly, and the ferroelectric polarizability is lowered in the case of samarium substitution. This fact is interesting regarding piezoelectricity by thereby increasing the ability to achieve a higher piezoelectric response. No results were achieved from ferroelectric and piezoelectric measurement due to the conductivity found in the sintered pellets were too high, probably due to secondary sillenite phases found in the material.

There has been found a finite size effect of a decrease in unit cell volume and tetragonality, of which the decrease in volume is contradictory to the expectations. There is also clear finite size effects on the decrease of cooperative displacement of cations, a measure for the polarization, and for the lowering of the ferroelectric phase transition temperature. The finite size effect for the ferroelectric phase transition has not been reported before. The magnetic phase transition temperature also show a decrease as a clear finite size effect. A linear relationship between electric polarization and magnetic ordering has also been observed in this project.

The results from this project contributes to the understanding of material properties of $BiFeO_3$ and derived compositions by an investigation of substitution effects and finite size effects. The results presented here motivates further research on these materials.

.

Preface

This project was done as a partial fulfillment of the requirements for the academic degree Master of Technology at the Department for Material Science and Engineering (IMT), Norwegian University for Science and Technology (NTNU).

This work is based on a project work by the author in the autumn of 2010, which together with this project is based on work done by Sverre Selbach in his Doctoral thesis.

Contents

.

1 Introduction

1.1 Background

The always increasing demand for performance of digital electronic memory devices has made studies on relevant materials popular [1]. One field that has been investigated recently is ferroelectric random access memory (FeRAM), which opens the possibility of smaller storage units [8, 9] and four-state memories by taking advantage of a combination of electric and magnetic polarization. A magnetoelectric [10] coupling takes this even further, offering the possibility to store data electrically and read them magnetically [14, 48].

Another important topic in modern materials science and engineering is lead-free piezo-electrics. The material used for electromechanical devices such as actuators, sensors and transducers in the industry today is lead-zirconate-titanate (PZT). The use of lead in industrial production is under strict regulation, beeing listed as a hazardous substance [12, 13]. Many countries, and the European Union, will prohibit the use of PZT as soon as replacement materials are available [11].

It is straightforward to conclude that knowledge and innovation within the two fields introduced above are of large scientific and commercial interest.

Bismuth ferrite, $BiFeO_3$, sometimes abbreviated "BFO", is perhaps the only material that is both mangetic and strong ferroelectric at room temperature [1, 15]. For this reason, $BiFeO_3$ is the most studied multiferroic material to this date. The recent interest in $BiFeO_3$ were stimulated initially by a paper by Ramesh et. al. [16] reporting a very high polarization and ferromagnetism. Other groups [17, 18] have reported that the ferroelectric and magnetic ordering in $BiFeO_3$ coincides, an observation leading towards magnetoelectric coupling. Selbach has reported that $BiFeO_3$ is thermodynamically stable, superior to competing materials [1, 22].

Thermal stability of lead-free piezoelectric materials have been a problem for most compositions, and gives $BiFeO_3$ a strong position in this respect. Although the piezoelectric response of $BiFeO_3$ being low [1], recent papers [20, 19] have reported that the piezoelectric response [25] of samarium substituted bismuth ferrite is strongly increased near the morpotropic phase boundary [20]. Most studies on piezoelectric $BiFeO_3$-based compounds have been on thin-films, and an understanding of the mechanisms present in the abscence of the strain-driven mechanisms in thin films is not yet established [21].

The compatibility of $BiFeO_3$ with Si and SiO_2, which are the base materials in the modern electronic industry, gives $BiFeO_3$ and derived compositions a strong position regarding an introduction to industrial-scale production processes [1].

This project is based upon the work done by Selbach [1] on bismuth ferrite, and is a continuation of the authors earlier study [3] of the material properties of bulk samarium substituted bismuth ferrite and their dependency on samarium substitution amount. Substitution with 10, 15 and 20mol% samarium showed that only the sample with the least substituted amount was phase-pure [3]. Based on this conclusion, the composition chosen for this finite size study is $Bi_{0.9}Sm_{0.1}FeO_3$.
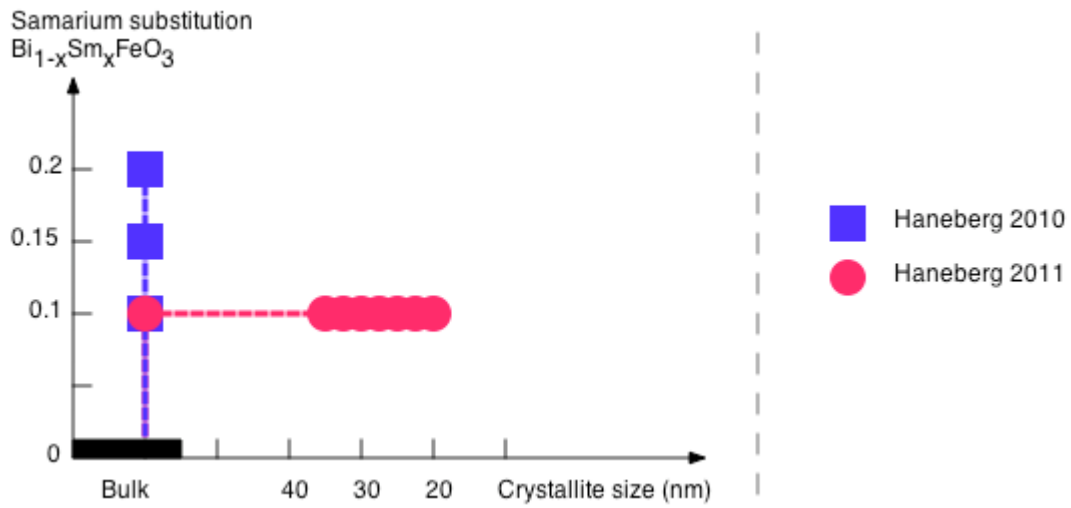
Figure 1: Diagram illustrating the connection between experiments by Haneberg 2011 (this text) and Haneberg 2010 [3]. Red dots and blue squares indicate the compositions in the respective experiments and the dashed lines indicate the axes of comparison. Bulk data for x=0 (unsubstituted $BiFeO_3$) is provided by Selbach [1].

1.2   Aim of work

The aim of this project was to further investigate the $Bi_{0.9}Sm_{0.1}FeO_3$ composition to study eventual changes in specific material properties as a function of crystallite size. The main focus is on the multiferroic and piezoelectric behavior, and hence the following properties are central in this study:

- Crystal structure - study the unit cell geometry and atomic positions and thus the origin of the material properties and how/if/why these changes. This will provide assumptions for actual material properties.

- Phase transitions with increasing temperature - study how the properties of the material changes as a function of temperature.

- Electrical measurements - electrical (ferroelectric) and electromechanical (piezoelectrical) tests to compare with theoretical assumptions.

In addition to these points, the synthetization of the material using a wet-chemical method will be studied and carried out, in addition to powder preparation and sintering prior to the electrical measurements.

The aim of this work is to do experiments on $Bi_{0.9}Sm_{0.1}FeO_3$ as nanoparticles and at bulk conditions to get a better understanding of the properties of this material. The results from this study will be compared with results from other studies, and will be discussed in this context.

It should be noted that even though the synthesis route, powder preparation and sintering are presented and discussed here, it is not the main focus of this text. These parts should be treated more like a description and discussion of appropriate tools nescessary the perform the desired experiments. This study is not a thorough investigation of synthesis methods, milling procedures and sintering schemes.

.

2 Theory

Properties that are central to $BiFeO_3$ and derived compositions, such as $Bi_{0.9}Sm_{0.1}FeO_3$, in addition to comparable materials, will be introduced in section 2.1. In section 2.2, a more detailed description on $BiFeO_3$ and rare-earth substituted $BiFeO_3$ will be given. Topics in synthetization of these materials that are relevant for this text is also presented in section 2.3.

2.1 Introduction to material properties

2.1.1 Polarization and ferroelectric effect

Polarization in a material is a difference in electric charge from one point to another, forming an electric field. Polarization may be due to a difference in electronic affinity between two species in the material. Polarization may also appear from a physical displacement and/or strain or as a result of an external electrical field. Many molecules are polar, a property which originates from the electronic structure of the molecule. A selection of these molecules may be used to create polarizable materials; materials that can posess a net polarization controlled by external forces [24].

The ferroelectric effect is an ordering phenomenon that originates from the fact that a group of materials can be polarized by an external field and posess a spontaneous polarization, i.e. ferroelectric ordering, in the abscence of such a field. This behavior provides a switchable net polarization [23], as illustrated in figure 2.
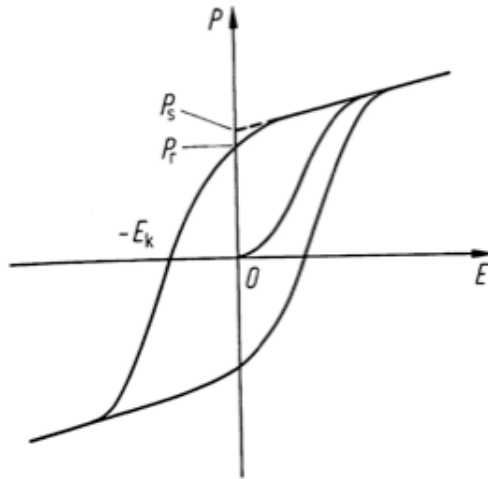
Figure 2: Ferroelectric switching behavior. P is the polarization and E the electric field P_s is the spontaneous polarization and P_r the remanent polarization in abscence of an external electrical field [23].

For ferroelectric behavior there exists an upper temperature limit, the Curie temperature T_C [5]. The polarizability of the material is given by the electrical susceptibility χ which is a variation of the dielectric constant $\varepsilon = \chi + 1$. Thus, the electrical susceptibility and dielectric constant are large in a good ferroelectric material. There is the following linear relationship between polarizability and dielectric constant [24]:

$$\mathbf{P} = \varepsilon_0 \chi \mathbf{E}, \text{ where } \chi = \varepsilon_0 - 1$$

The most common mechanism for polarization in ferroelectrics is displacements of cation species in relation to the anions in the crystal. The material is polarized when an external electrical field displace one or more cations in the unit cell. A material may be polarizable, but in order to provide a spontaneous polarization some sort of stabilization in the polarized state is needed [25]. If stabilization is nonexistent, the displaced cations will return to their neutral state when the external field is removed.

The most common stabilization meachnism for ferroelectrics is partial covalent bonding between the displaceable cation and the anion sublattice [1]. In perovskites, this stabilization occurs between the empty d orbitals of a cation, for example Ti^{4+} in $PbTiO_3$ or Fe^{3+} in $BiFeO_3$, and 2p orbitals of the oxygen anions. If there exist electron lone-pairs at the other cation these will also contribute to the stabilization, for example the lone pairs of Bi^{3+} in $BiFeO_3$ [15].

For ferroelectric stabilization to be possible, the unit cell must be stretched in at least one direction, i.e. it must be non-centrosymmetric. The resulting inversion asymmetry must be the case to acheive a net polarization in the system. Ferroelectrics like $PbTiO_3$, $BaTiO_3$ and $BiFeO_3$ have a tetragonal (cubic but with an elongated c parameter) structure in their ferroelectric phase [26]. At this point the crystallographic origin of T_C comes into account as these materials transform to a cubic, and therefore centrosymmetric, structure at T_C and higher temperatures. The possibility of an off-centered cation is then lost, and hence the ferroelectricity. A material in this state is called paraelectric. The effect of this phase transition is illustrated in figure 3, in this case for lead titanate, $PbTiO_3$.
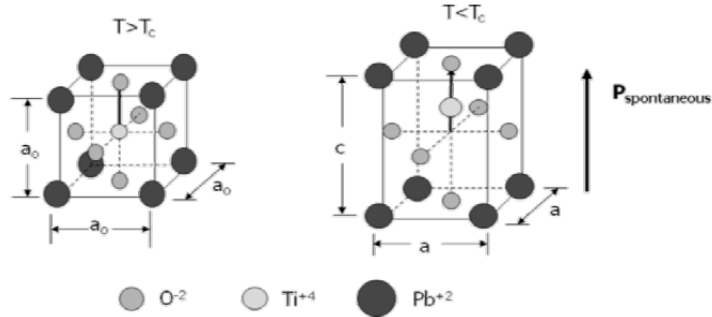

Figure 3: Illustration of the high temperature cubic phase (left) and low temperature tetragonal phase (right) for a ferroelectric perovskite, in this case lead titanate [24].

2.1.2 Ferromagnetism

Analogous to ferroelectricity, ferromagnetism is the existence of a spontaneous magnetization, also switchable by an external magnetic field [5]. The origin of ferromagnetic ordering effect is the ordering of electronic spins of d an f orbital unpaired electrons in the material, and ferromagnetism is lost at and above the Curie temperature T_C. Ferromagnetism exists in metals such as iron and cobalt, but is seldom found in perovskites [1]. In contrast, antiferromagnetism is existent in perovskites such as $BiFeO_3$ [15]. In an antiferromagnet, the electron spins are antiparallell, resulting in no net magnetization. However, in the case of a perovskite, the spins of the B cations, such as Fe^{3+} in $BiFeO_3$, may couple and align parallell trough the oxygen anions trough so-called electron superexchange [7] which obeys Hunds rule of electronic spins. Analogous to ferromagnetism, an upper thermal limit for antiferromagnets exists; the Neel temperature, denoted T_N. Above T_N, a material is commonly paramagnetic [5].

2.1.3 Piezoelectricity

The piezoelectric effect is a relationship between mechanical stress and a change in polarization in materials which has this ability [23]. There are two types of piezoelectric effects; the direct piezoelectric effect and the converse piezoelectric effect [25]. The direct effect is based on an applied stress T which will induce a change in the polarization P in a linear relationship $P_1 = d_{111}T_{11}$, where d is the piezoelectric coefficient which is a constant property of a system. Likewise, the piezoelectric coefficient gives the relationship between the polarization due to an applied electric field E and the induced strain S; $S_{11} = d_{111}E_1$. The two piezoelectric effects are illustrated in figure 4.

The subscript numbers in the denotation for the piezoelectric coefficient describes the relationship between the direction of the mechanical stress or strain and the polarization [25]. The first number is the polarization direction(s) and the second is the stress/strain direction(s). The numbers denote the three cartesian axes (1="x",2="y" and 3="z") while the numbers 4, 5 and 6 used for the mechanical component descibes shear planes. For example, d_{11} descibes a polarization parallell to the applied stress while d_{12} describes polarization perpendicular to the applied stress.

Analogous to the ferroelectric effect, a material needs to be non-centrosymmetric for the piezoelectric effect to exist [25]. The reason for this is that deformation will only contribute to polarization if the displaced charges does not cancel each other out.
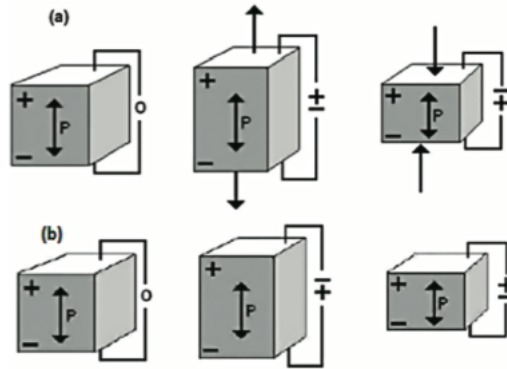
Figure 4: a) Direct piezoelectric effect and b) converse piezoelectric effect [25].

While many materials have the possibility of piezoelectric behavior, the effect is for most materials weak. Also, the microstructural mechanisms for piezoelectricity is not well understood. However, in general, the meachism can be roughly explained by a displacement of charged species by deformation of the material. When mechanical stress is applied, this stress will result in either compression along one or more axes, elongation along one or more axes, or both simultaneously. Compression or elongation will displace charged species and therefore change the polarization. Regarding the converse piezoelectric effect, a displacement of charged species by an electrical field will force stress in the material, and if strong enough, result in deformation along one or more axes.

2.2 Introduction to BiFeO$_3$ and Bi$_{(1-x)}$Sm$_x$FeO$_3$

Pure bismuth ferrite may be modified in several ways. An important route to modify its properties is to substitute bismuth with another cation, such as a rare-earth metal. Samarium is a rare-earth metal which differs from bismuth with its much smaller ionic radii and the fact that samarium does not have lone pairs like bismuth.

2.2.1 Crystal structure

Bismuth ferrite, BiFeO$_3$, is a multiferroic material with the perovskite ABO$_3$ structure. Since both the iron and bismuth cations are trivalent, Fe^{3+} and Bi^{3+}, respectively, BiFeO$_3$ is called a III-III perovskite. The structure consists of an Fe^{3+} cation inside an O$_6$ oxygen anion octahedron. The vacancies between the octahedra are filled with Bi^{3+} anions. The structure is illustrated in figure 5.
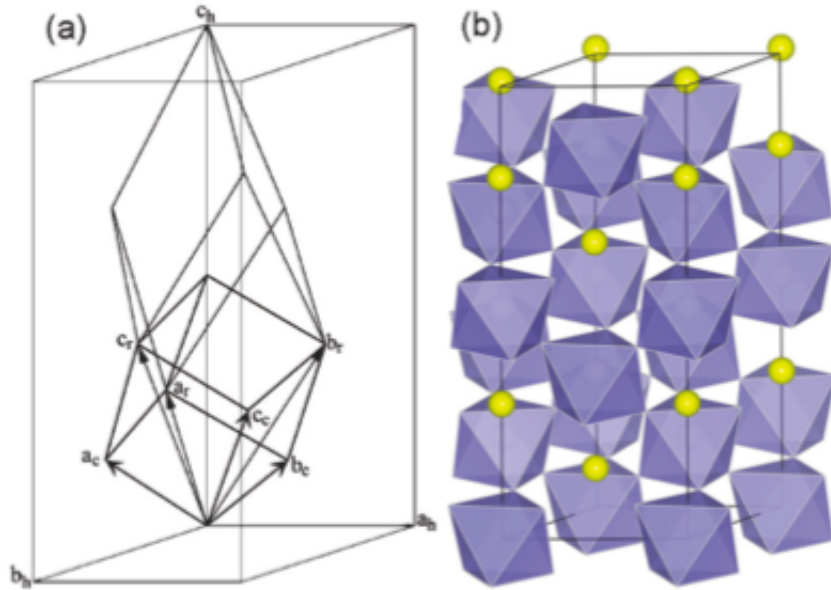

Figure 5: Illustration of the BiFeO$_3$ perovskite crystal structure [1]. a) Relationship between cubic (c), rhombohedral (r) and hexagonal (h) unit cell directions. b) Hexagonal unit cell with oxygen octahedra (blue) and bismuth cations (yellow).

In bulk BiFeO$_3$, the structure is rhombohedrally distorted due to octahedra tilting around the $[001]_{hex}$ axis [29, 27, 26], as discussed in section 2.1.2. The hexagonal unit cell parameters og bulk size BiFeO$_3$ are a$_{hex}$=5.5787Å and c$_{hex}$=13.8688Å [26].

The comparative sizes of the ions in the BiFeO$_3$ structure is important for the stability of the structure. The relations between ionic radii can be denoted by the Goldschmidt tolerance factor [51], assuming the ions are round spheres, given for a perovskite as;

$$t = \frac{r_A + r_O}{\sqrt{2}(r_B + r_O)} \ [1]$$

where r$_A$ is the A cation radii, r$_B$ is the B cation radii and r$_O$ is the radii of the oxygen O^{2-} anions. In BiFeO$_3$, Bi^{3+} is the A cation and Fe^{3+} is the B cation. The Bi^{3+} is too

small to properly fill the vacancies between the octahedra. This results in a tolerance factor t of lower than unity and R3c space group. For bulk $BiFeO_3$, t=0.890. The tetragonal and rhombohedral distortions from an ideal cubic perovskite structure originates from the reduced tolerance factor [50]. Upon further reduction of t below t=0.86, the structure will become unstable and transform towards hexagonal structure. When the cations do not perfectly fit the ideal cubic structure, the oxygen octahedra will be tilted by an angle θ to fit into the lattice. In the case for pure bulk $BiFeO_3$, this angle is 11°-14° [15, 27].

Effect of substitution and size The samarium ion, Sm^{3+}, has an ionic radii of 1.132Å which is considerably smaller compared to the 1.365Å ionic radii of Bi^{3+}. This further reduces the tolerance factor from the value for pure bismuth ferrite, with reference to the equation above. Therefore there is a limit for the amount of samarium substitution before a phase transition occurs [1]. To better compare the distorted structure with the ideal cubic perovskite structure, the unit cell parameters can be normalized by using:

$$a_{norm} = \left(1/\sqrt{2}\right) a_{hex} \text{ and } c_{norm} = \left(1/\sqrt{12}\right) c_{hex} \text{ [1]}$$

Using these two relations gives the following for:

Composition	a_{hex}	c_{hex}	a_{norm}	c_{norm}
$BiFeO_3$	5.5787Å	13.8688Å	3.9447Å	4.0036Å
$Bi_{0.9}Sm_{0.1}FeO_3$	5.5665Å	13.7974Å	3.9361Å	3.9830Å

Table 1: Hexagonal and normalized unit cell parameters for pure bismuth ferrite and 10 mol% samarium substitution [3].

The values from table 1 gives the following relations:

$$\frac{a_{hex}(Bi_{0.9}Sm_{0.1}FeO_3)}{a_{hex}(BiSmFeO_3)} = 0.9978 = 99.8\% \text{ and } \frac{c_{hex}(Bi_{0.9}Sm_{0.1}FeO_3)}{c_{hex}(BiSmFeO_3)} = 0.9948 = 99.5\%$$

Because polarization is along the c-axis for $BiFeO_3$, the so-called tetragonality, the relationship c_{hex} / a_{hex} is an important structural and functional property of the material [1]. Substitution of bismuth by smaller cations such as rare-earth metals [55], among them samarium, has been shown to decrease the tetragonality of the structure, which results in a more cubic crystal structure [1]. This effect is due to the fact that the rare-earth cations do not have $6s^2$ lone-pair electrons like Bi^{3+} and the tetragonal polar structure will therfore be weakened, this is presented further in the next sections.

Upon substitution, a phase transition will occur at a certain level for a given rare-earth element. A phase transition to orthorombic structure occurs at approx. 15mol% for Sm substitution [59] and at approx. 20mol% for La and Nd substitution [19]. Experimental tests using electron diffraction have shown a relationship between decreasing susbstituent ionic radii and a decreasing substitution amount before a phase transition occurs [19]. Regaring size effects, when approaching small enough crystallite sizes, the c_{norm} / a_{norm} measure is approaching unity [1, 21].

2.2.2 Ferroelectric properties

Pure $BiFeO_3$ will polarize along the $[001]_{hex}$ axis by a displacement of Bi^{3+} and Fe^{3+} cations of a distance of s and t, respectively. This is illustrated in figure 6. The difference between these distances will result in a net polarization in the unit cell, closely couplet to the value for T_C [28]. Experimental studies have reported the spontaneous polarization P_s of $BiFeO_3$ to be in the 90-108$\mu C/cm^2$ range [15], which is large compared to other materials such as $BaTiO_3$ and $PbTiO_3$. The strong polarization is due to the large displacements of the cations [19] in $BiFeO_3$ correlated with its high Curie temperature at 830°C [26, 32]. Discussed in section 2.1.1, some of the stabilization in $BiFeO_3$ originates from the partial covalent bonding between Fe^{3+} d orbitals and O^{2-} 2p orbitals. Bi^{3+} has 6s^2 lone pairs which will also create a partial covalent bonding with the same oxygen electrons in the octahedron, which offers the main stabilization in pure BiFeO3 [15], accounting for approximately 98.5% of the total spontaneous polarization [49]. An effect due to the fact that the spontaneous polarization is large compared to other materials, the energy needed to overcome the stabilization and switch the polarization will also be higher. Along the $[001]_{hex}$ axis, polarization has been deduced to be 60$\mu C/cm^2$ through experiments on single crystals [62].
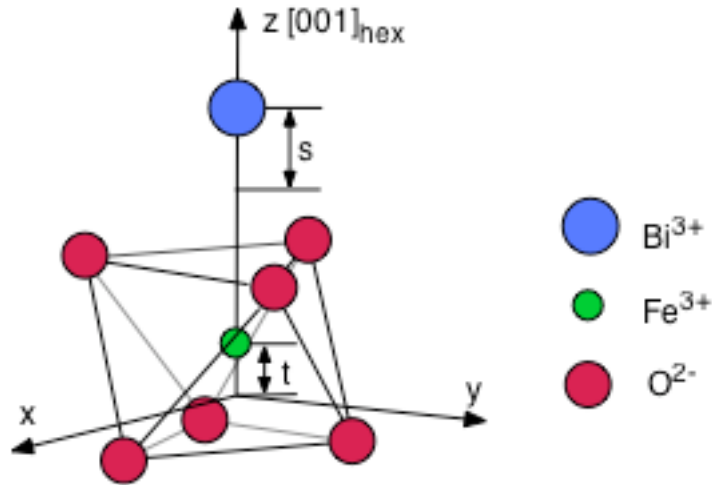

Figure 6: Illustration of polarization in $BiFeO_3$ perovskite from difference in displacements s and t.

Effect of substitution It has been reported by several groups that rare-earth substitution of Bi^{3+} will reduce the stabilization energy of the ferroelectric polarization [19, 20, 38]. The structural background for this is that an ion without lone pairs will not bond as strongly as Bi^{3+} to the octahedra and therefore lower the polarization threshold potential, comparable with the substitution effects found on tetragonality [1]. The ferroelectric phase transition is strongly dependant on rare-earth substitution, with reference to the T_C of pure $BiFeO_3$ at 830°C and reported T_C of $Bi_{0.9}Sm_{0.1}FeO_3$ at 448°C [19]. The same trend is also appearent for other cations (La, Nd, Gd), and T_C decreases with increasing substitutant concentrations [19, 27]. An overview of experimental data from Karimi et.al. is presented in table 2 and figure 7.

Karimi et. al. also presents the correlation between tolerance factor and Curie tempera-

ture, presented in figure 8. As the tolerance factor is derived from ionic radii, the relationship between t and T_C is also a relationship between substitutant cation radii and T_C, with reference to section 2.2.1.

It should be noted that although rare earth-substitution can induce desired effects on ferroelectric effects in bismuth ferrite, a drawback in electrical properties of Sm-substitution can be that experiments [38] have shown that the leakage current is higher in Sm-substituted bismuth ferrite than in the pure compund, in many cases limiting practical applications [11].

RE cation	Substitution x	Average tolerance factor	Curie temperature, T_C
-	0	0.96429	830^oC
La	0.05	0.96375	754^oC
La	0.10	0.96321	677^oC
Nd	0.05	0.96286	696^oC
Nd	0.10	0.96143	518^oC
Nd	0.15	0.96	325^oC
Nd	0.20	0.95857	170^oC
Sm	0.05	0.96232	677^oC
Sm	0.10	0.96036	448^oC
Sm	0.15	0.9584	309^oC
Gd	0.05	0.962	652^oC
Gd	0.10	0.959	372^oC

Table 2: Effects on the ferroelectric phase transition as a result of rare-earth (RE) substitution [19].
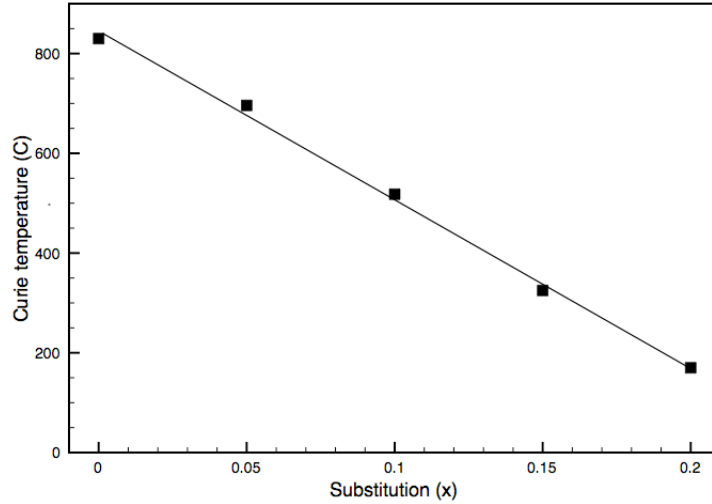

Figure 7: T_C as a function of Nd-substitution in $Bi_{1-x}Nd_xFeO_3$ by Karimi et. al. [19]
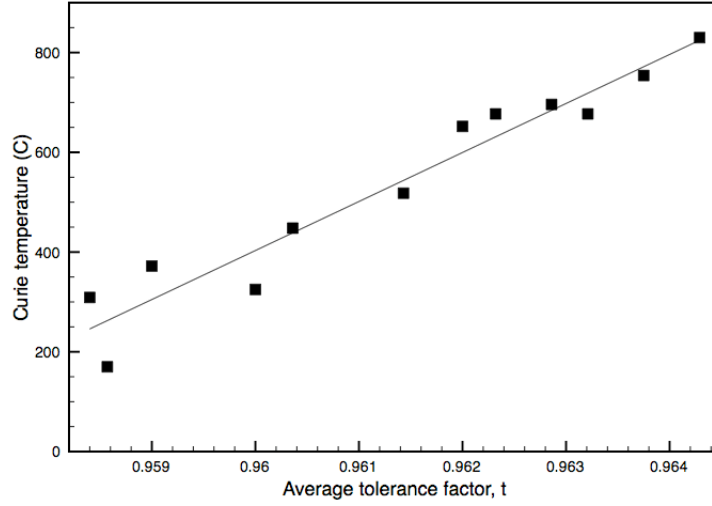
22

Figure 8: T_C as a function of average tolerance factor by Karimi et. al. [19]

Size effects   The ferroelectricity in $BiFeO_3$ arises from the competition between long-range and short-range electrostatic forces. The short-range forces facilitates paraelectricity, while long-range forces alignment of polarized dipoles, and thus an increase in the net polarization [1]. When crystallite size is decreasing below a certain level, the long-range electrostatic stabilization forces in the material are restricted [1]. In such small nanoparticles, there will still be dipoles due to polarity of partial covalent B^{3+}-O^{2-}bonds, but their alignment are lost. Experiments [1] found that the displacement of Fe^{3+} increases more than the displacement of Bi^{3+} which can be attributed to the loss of long-range electrostatic forces upon a decrease in crystallite size[1].

2.2.3 Piezoelectricity

In displacive ferroelectrics like $BiFeO_3$, piezoelectric effect will result from an applied stress as domain wall movements changing the polarization direction [24], as illustrated in figure 9.
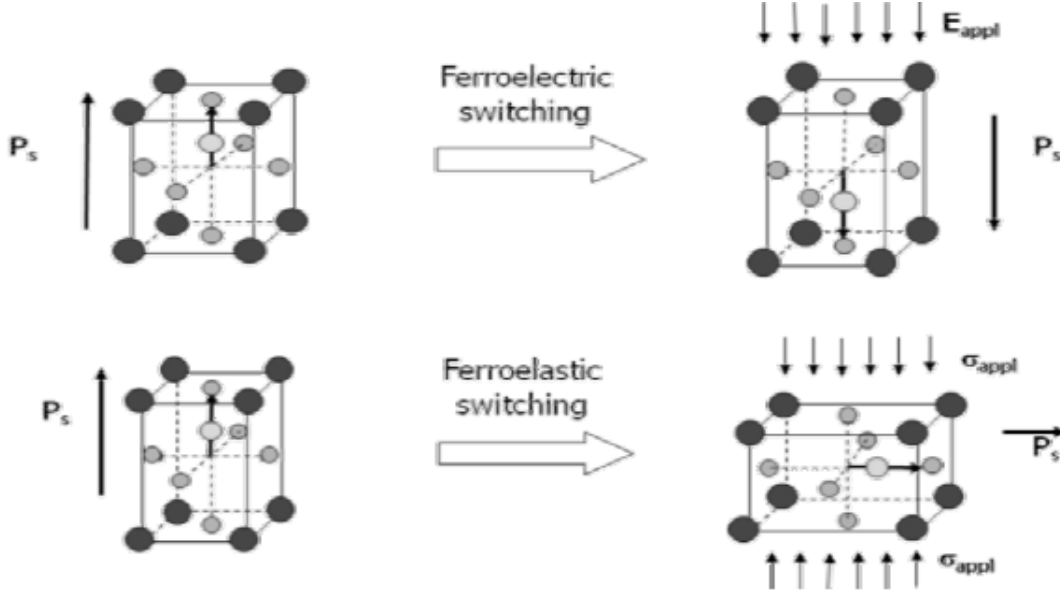

Figure 9: Polarization switching in perovskite by a sufficiently strong electric field (upper) and by a sufficiently strong mechanical stress (lower) [24].

Compared with the large polarization of $BiFeO_3$ [1], its piezoelectric response d_{33} is weak, experimentally reported to be in the 15-60pm/V range [16, 47, 62]. For bulk single-crystal $BiFeO_3$, a d_{33} of 70 pm/V have been reported [62]. To set this in perspective, conventional lead-based polyscrystalline piezoelectric materials provide a piezoelectric coefficient of 100-200 pm/V [1].

Effect of substitution Although the piezoelectric response of pure $BiFeO_3$ is low, Sm^{3+} substitution of bismuth has shown to increase the piezoelectric response with a peak of 110 pm/V [20] at the morphotropic phase boundary at x=0.14 in room temperature for $Bi_{1-x}Sm_xFeO_3$ for thin-films [20, 46].

As already mentioned, the Curie temperature for rare-earth substituted $BiFeO_3$ has been shown to be considerably lower than for the pure compound. A combination of data for T_C and d_{33} for a variation of piezoceramics emphasize the importance of T_C on the piezoelectric response, presented in figure 10.
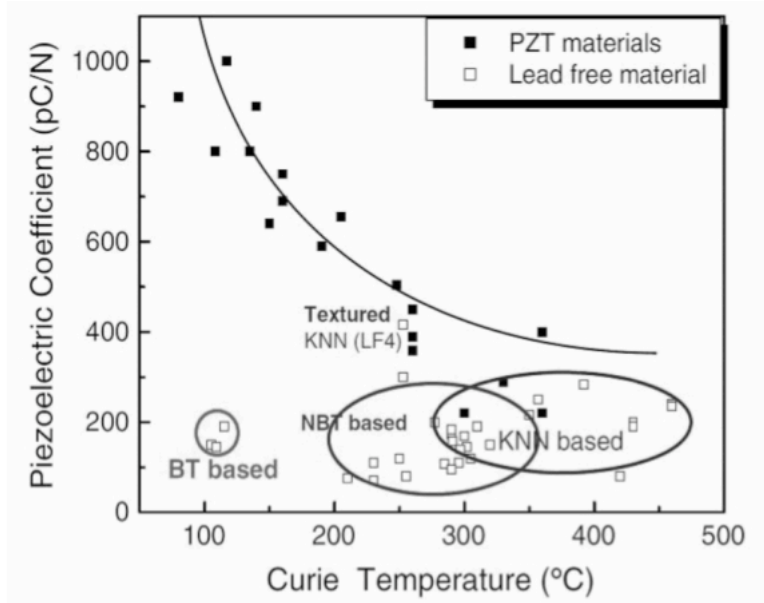
Figure 10: Room temperature values of d$_{33}$ as a function of T$_C$ for various piezoceramics [6].

The clear trend visible in figure 10 with increasing d$_{33}$ upon a decrease in T$_C$ states the importancy of lowering the polarization in BiFeO$_3$-based materials for piezoelectric applications.

2.2.4 Magnetic properties

Bismuth ferrite is G-type antiferromagnetic [34] where the Fe^{3+} ions are surrounded by six nearest neighbours with the opposite spin. BiFeO$_3$ becomes paramagnetic through a magnetic phase transformation at 370°C for pure bulk BiFeO$_3$ [15, 26, 32]. Since the oxygen octahedras of BiFeO$_3$ are tilted by an angle θ, the antiferromagnetic response is higher than for Fe-O-Fe angles of 180°, this angle being 154°-156° for pure bulk BiFeO$_3$ [15]. In short; the antiferromagnetic response increases as a result of octahedra tilting. This tilting angle θ thus impacts T$_N$ by the following relation [1]:

$$T_N \propto cos^2\theta$$

By using this relation, an increasing tilting angle will decrease the Neel temperature.

Octahedra tilting will also result in a weak net ferromagnetic reponse locally [18], as illustrated in figure 11. Illustrated in figure 12 this net response will cancel out on average with a periodicity of 62-64nm [15, 29, 62].
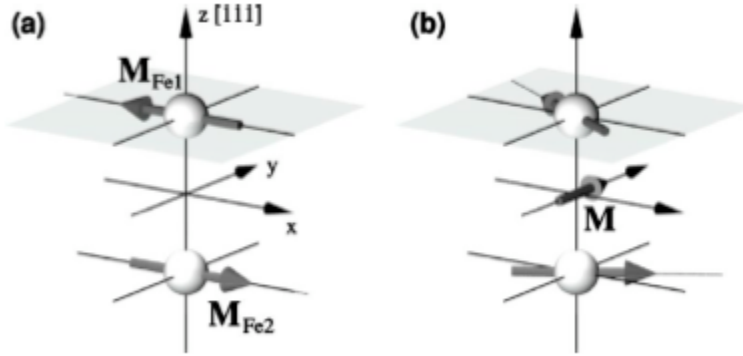
25

Figure 11: a) Antiferromagnetism by opposite magnetic spins and b) tilted structure will induce a small net ferromagnetic moment as the difference in antiferromagnetic spins, denoted by vectors **M**, between two iron cations, Fe1 and Fe2 [18]. Net ferromagnetic moment is denoted **M** in figure b).
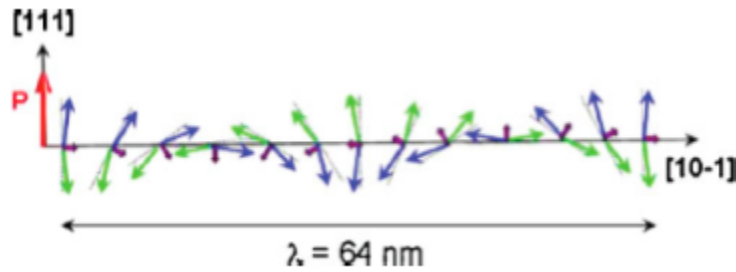

Figure 12: Weak ferromagnetic moment (purple) from rotating antiferromagnetic moments (blue/green) [41].

Effect of substitution Introduction of magnetically active rare-earth metals such as Sm, La and Nd in $BiFeO_3$ is considered an effective way to improve the magnetic properties of the perovskite [59]. Substitution of lanthanum, La^{3+}, for Bi^{3+} in $BiFeO_3$ has been shown to improve the magnetic response [61]. The same trend has been reported for Nd^{3+} substitution [60], but the large increase in magnetic response appears from 15mol% Nd substitution and up, however, a remanent magnetization M_r of 0.015 emu/g were reported for $Bi_{0.9}Nd_{0.1}FeO_3$.

Size effects Upon decreasing particle sizes for single-crystal $BiFeO_3$ nanoparticles, the ferromagnetic response has been reported to largely increase at diameters below 62nm, the periodicity of the rotating spin-induced magnetic moments [32, 33]. Its origin is that the magnetic moments will not cancel each other out like in bulk material, reaching maximum magnetization of 1.55 emu/g and remanent magnetization M_r of 0.031 emu/g for 14nm crystals at room temperature [33]. For such small crystals, the surface to value ratio will be large, and surface strain and uncompensated electron spins will affect the magnetic response. Experimental results [32] for this is given in figure 13 for $BiFeO_3$ nanoparticles with 110-160nm diameter compared with bulk $BiFeO_3$.
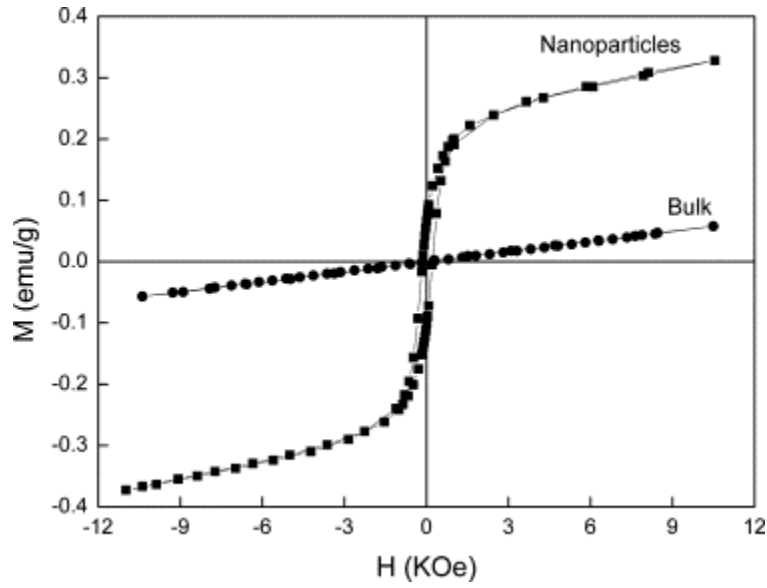
Figure 13: Magnetic hysteresis for 110-160nm BiFeO$_3$ nanoparticles and bulk BiFeO$_3$ [32].

2.2.5 Domains and domain walls

In polycrystalline BiFeO$_3$, ferroic ordering is divided into domains. A domain is defined as a restricted volume in the material where for example the ferroelectric polarizations all have the same direction. The borders between such domains are called domain walls. Domains and domain switching are illustrated in figure 14.
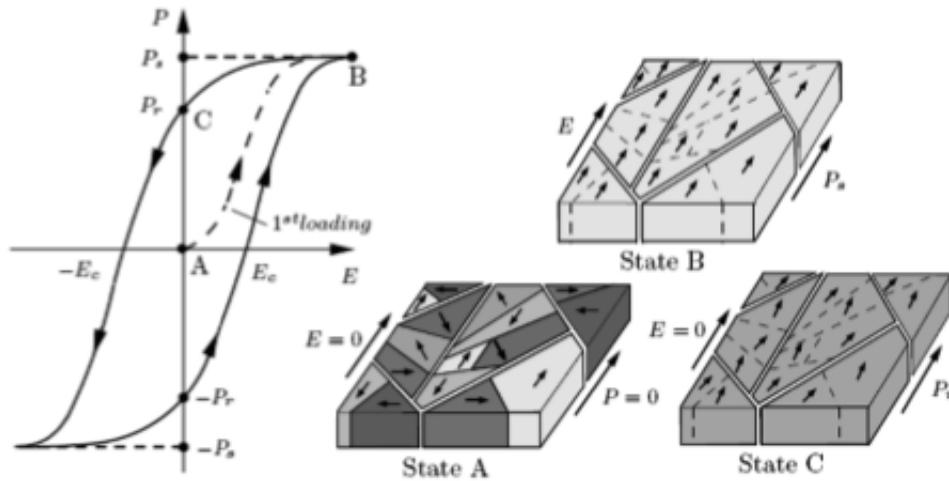

Figure 14: Domain wall movement related to ferroelectric switching [24].

In BiFeO$_3$, there are three types of domain walls, named after the angle between polarization vectors on either side of the wall [15]:

- 71° domain walls: Assume the polarization is along the $[111]_{cub}$ axis on one side of the wall and along the $[11\bar{1}]_{cub}$ on the other. The angle between two polarization vector where only one component is reversed will be approximately 71°.

- 109° domain walls: The angle between two polarization vector where two components are reversed is approximately 109°.

- 180° domain walls: A domain wall where the polarization on one side is reversed with respect to the other side, which are along the $[111]_{cub}=[001]_{hex}$ polar direction in the perovskite.

A switch in polarization can be regarded as movement or growth of ferroelectric or magnetic domains. Piezoelectric behavior is also due to strain induced from movement of 71° and 109° domain walls, or vice versa. The 180° ferroelectric switching does not require ferroelastic deformation and will thus not induce ferroelastic strain [43], which is on the other hand is the case for 71° and 109° domain walls [1]. In small electric fields, the domain wall displacements will only be negligible affected, but in a large enough electric field, the domain wall displacements will be partially irreversible, and therefore result in piezoelectric hysteresis, depending on the piezoelectric coefficient [44].

Since there exists three types of ferroic order in BiFeO$_3$, domains can be divided into ferroelectric domains, antiferromagnetic domains and ferroelastic domains. These three are however not independent in BiFeO$_3$, where the ferroelectric domains are restricted by the ferroelectric strain states in the material, and antiferromagnetic and ferroelectric domains coincide with each other [1], dicussed briefly in the next section.

2.2.6   Magnetoelectric coupling

Magnetoelectric coupling is a phenomenon which makes magnetic and electric ordering impact each other, in other words; couple them. BiFeO$_3$ has strong polarization but only weak ferromagnetism, as discussed above. Since the magnetic susceptibility is very low, the magnetic ordering is diffcult to control directly. However, the magnetoelectric coupling found in BiFeO$_3$ [1, 40] open up a new possibility in this respect [21]. By ferroelectrically switching the oxygen octahedra rotation direction, a theoretical study [18] found that the ferromagnetic moment can be reversed. The same study also found that switching the Bi^{3+} and Fe^{3+} displacements did not affect the ferromagnetic moment. It has been shown by two studies that a 71° polarization switching resulted in a similar switching of the magnetization [17, 41], illustrated in figure 15. It has also been proposed that the magnetoelectric coupling originates from magnetostriction and piezoelectricity [42].
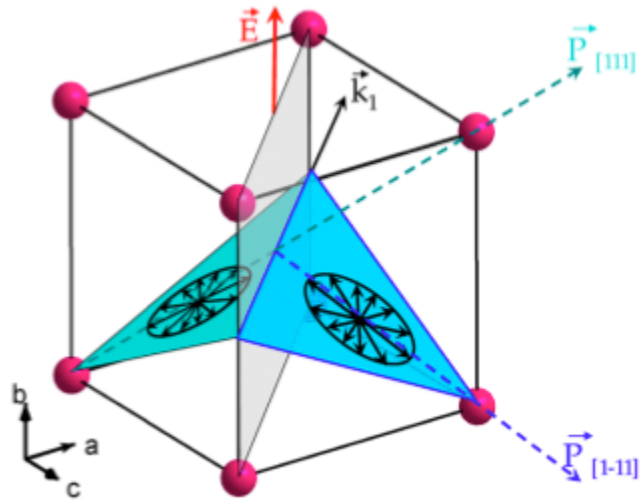
Figure 15: Figure illustrating a 71º domain wall (grey). Polarization vectors $\vec{P}$, plane of magnetic spin cycloid and the propagation vector $\vec{k}$ are shown [41].

2.3 Synthesis

There are two common routes applicable to synthesize $BiFeO_3$ ceramic powders [1]; 1) solid-state and 2) wet-chemical.

The solid-state method is basically to grind excact stochiometric amounts of bismuth and iron oxide together and then calcine at for a given time and temperature in normal or controlled atmosphere [1]. The main challenge in this method is to achieve a homogeneous mixing of the two cation species. On the other hand, precipitation from liquid phase is not an issue, as it is in the wet-chemical route.

The wet chemical synthesis route starts out with cation precursor solutions and an organic solution [1]. The bismuth and iron precursor solutions are mixed in stochiometric amounts and the organics is added to make a gel skeleton around the cations. There are a range of solvents applicable to this method. As the wet-chemical route is the one relevant for this text, since it does not require the high calcination temperatures of a solid state synthesis, which may result in large crystallites [1]. The wet-chemical synthesis will therefore be further discussed here.

2.3.1 The Pechini synthesis

The Pechini [35] syntesis is a widely used method to synthesize nanocrystalline ceramic powder [30, 57]. Its advantages are that no expensive or special equpiment is needed; it is cheap, it is relatively stable and homogeneous nanosized particles can be acheived easily [29]. The Pechini method is a sol-gel synthesis method, which, as the name implies, involves a polymer gel in a solution.

The theory in the Pechini synthesis is that every cation is to be catched by the polymer newtwork formed in the solution, forming a gel. When the gel has dried, there will be a polymer skeleton holding the cations in place. An illustration is given in figure 16. Upon heat treatment at higher temperatures, this polymer is burnt off, allowing the cations to react and form polycrystalline nanoparticles. Since the heat treatment is done in normal atmosphere, the cations will also react with oxygen, forming an oxide, such as bismuth iron oxide; $BiFeO_3$.

Carboxylic acids are often used for the polymer network, figure 16 shows examples for such network by using tartaic and citric acids.

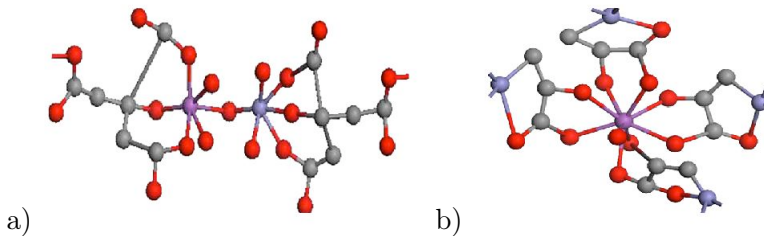

a)   b)

Figure 16: a) Citric and b) tartaric carboxylic acids forming a polymer network [29] Iron=blue, Bismuth=purple, Oxygen=red and Carbon=grey.

There are several variables that need to be controlled when using the Pechini method to syntesize bismuth ferrite:

- Correct stochiometry - even a small stochiometry error will result in the formation of secondary phases, with reference to the phase diagram in figure 17.

- Solubility conditions - cation nitrates must be completely soluble in the solution to avoid precipitation which leads to inhomogenity.

- Total complexation - all cations must be complexated by the complexing acid.

- Homogenity - the solution must be homogenious to achieve phase-pure material.

Stochiometry The phase diagram in figure 17 illustrates the fact that the stochiometry of the cations (Fe^{3+}, Bi^{3+}) with respect to each other must be accurate. A small surplus of Bi^{3+} will result in bismuth oxide, Bi_2O_3, or the very similar sillenite, $Bi_{25}FeO_{39}/Bi_{25}FeO_{40}$. On the other hand, a Fe^{3+} surplus will initiate formation of iron-rich phases such as mullite, $Bi_2Fe_4O_9$ [1].

Although such secondary phases are assumed to have little or no impact on the crystal structure on the $BiFeO_3$ R3c phase, it may render the measured properties of the material or in the worst case make such a measurement impossible or useless [33]. For example, sillenite, which conducts electrons much better than bismuth ferrite will result in high leakage currents in electrical measurements for ferro- and piezoelectric properties.
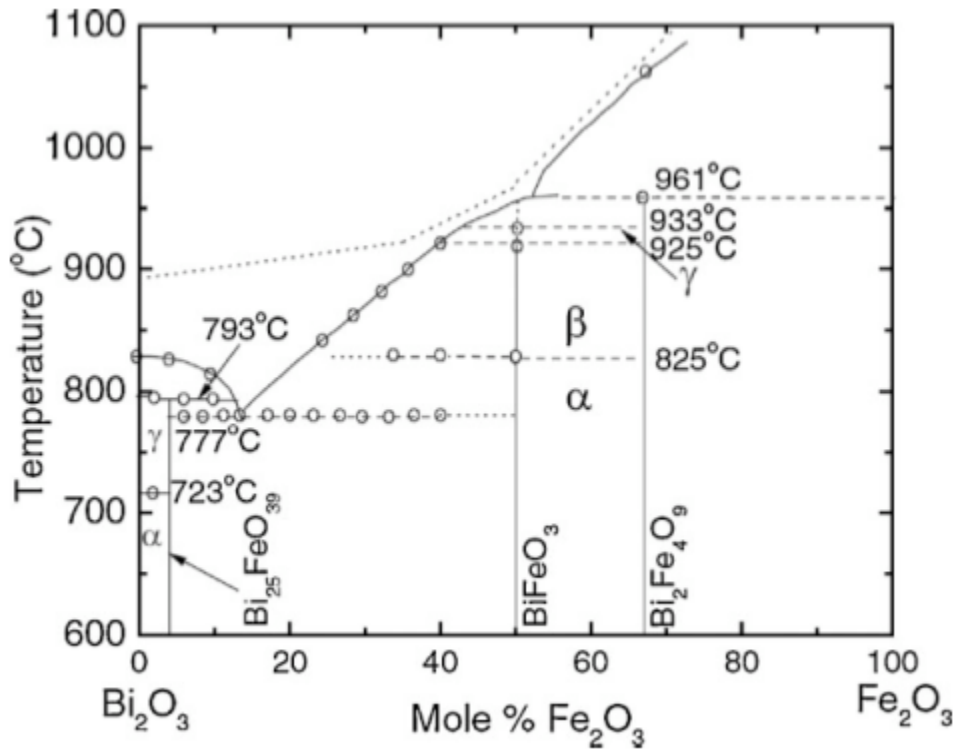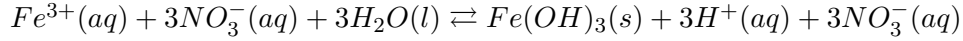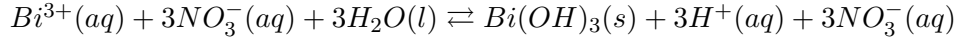

Figure 17: Phase diagram of pure $BiFeO_3$ [37].

Rare-earth substitution, even at low levels ($\leq 10mol\%$) is known to reduce the occurance of secondary phases [58] by stabilizing the perovskite structure due to stronger Sm-O bonding compared to Bi-O in pure $BiFeO_3$ [38]. The larger free energy the formation of Sm-O bonds gives, the more perovskite formation is facilitated, assuming negligible contribution from entropy change since the Sm^{3+} cations are randomly distributed [38].

Solubility For the solved bismuth and iron nitrate in water, the following equilibria exists:

$$Bi^{3+}(aq) + 3NO_3^-(aq) + 3H_2O(l) \rightleftarrows Bi(OH)_3(s) + 3H^+(aq) + 3NO_3^-(aq)$$

$$Fe^{3+}(aq) + 3NO_3^-(aq) + 3H_2O(l) \rightleftarrows Fe(OH)_3(s) + 3H^+(aq) + 3NO_3^-(aq)$$

From these, it is appearent that a low pH is nescessary to drive the equilibria to the left and give better solubility [31, 62]. From other experiments [56], there have been reported that the pH for the iron nitrate precursor must be in the pH=1-2 range or lower and for bismuth even lower at around 1 or lower. This must be held for the whole synthesis route. Nitric acid has the following equation for dissolving in water;

$$HNO_3(l) + H_2O(l) \rightleftarrows H^+(aq) + NO_3^-(aq) + H_2O(l)$$
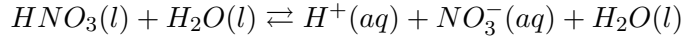
and are therefore applicable to this synthesis since the nitrate remains are the same as from the cation precursor solutions and will thus not affect the material outcome or form any extra by-products, and also drive the solution equilibria to the left. The carboxylic acids used for complexation are weak and their effects on pH is negligible compared to a strong acid such as HNO_3 [1].

Complexation One of the key points of the Pechini synthesis is the possibility to achieve very small crystallites [57]. This is dependent on the complexation of the cations forming the gel, as the polymer network hinders the cation species in forming bulk crystallites. A good polymer network will provide crystallite growth until it may be burnt away in the 300-400°C temperature range. If total complexation is not the case, unwanted crystallites will form and grow and therefore the ability to control material crystallite size vanishes.

Homogenity The global stochiometry in the solution may be right, but if the solution is not homogenious, there will form local stochiometry errors [1]. Assumed that all cations are fully complexated, these local errors will not influence the material until it is heat treated to a temperature where the polymer skeleton is burnt away. If there are any local stochiometry errors, unwanted secondary phases may form in the same manner as if there were a global stochiometry error in the solution [32].

2.3.2 Heat treatment

In a dried gel, the polymer network is still surrounding the ions. To make the ions oxidate and form crystallites, the dried systhesis product need, as already mentioned, to be heat treated to burn off organic components and for the ions to react. For carboxylic acids such as citric or tartaric acid, this happens at approximately 350^oC [29, 30], also presented by thermogravimetral (TG) plots in Appendix B.

It has been reported [29] that citric acid will lead to earlier crystallization during calcination and therefore the possibility to make smaller nanoparticles than if tartaric acid is used. The differences between these two are illustrated by XRD diffractograms in Appendix B.

However, taken into account that citric acid polymer increase the possibility for a combustion process during heating of the solution or during calcination, control over crystallite growth may be lost. A combustion process of this type, called auto-ignition[30], will result in higher local temperatures, and the crystallites may therefore grow more than what would be expected from the heating or calcination temperature [30]. Auto ignition can also, according to the same group, lead to formation of impurity phases, such as sillenite $Bi_{25}FeO_{39}/Bi_{25}FeO_{40}$, mullite $Bi_2Fe_4O_9$ and bismuth oxide, Bi_2O_3 [30].

Thermal stability   These impurity phases, which are the most dominant in $BiFeO_3$ powders, may also be formed from the perovskite phase by the following reaction [1]:

$$\frac{12}{49}Bi_2Fe_4O_9 + \frac{1}{49}Bi_{25}FeO_{39} \rightleftarrows BiFeO_3$$
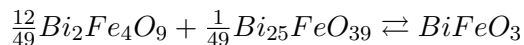
The left hand side of this equation is experimentally shown to be increasingly favorable upon heating until 817^oC is reached [1]. Impurities such as alumina, Al_2O_3, and silica, SiO_2, are more soluble in sillenite and mullite phases and will therefore drive the equality to the left. Unfortunately, these impurities are common in materials that contacts $BiFeO_3$ in experiments and may therfore contribute to secondary phase growth. Selbach [1] proposed that the formation of the two secondary phases upon heating was due to chemical incomatibility with materials in contact with the powder and not due to an intrinsic instability of $BiFeO_3$ [1].

The volatile nature of Bismuth [1, 26] may result in a bismuth deficiency at higher temperatures ($>600^oC$). The excess of iron this leads to will facilitate the formation of iron rich phases, such as $Bi_2Fe_4O_9$, with respect to the phase diagram in figure 17.

.

3 Experimental

3.1 Synthesis and sintering

3.1.1 Precursor solutions

Precursor solutions were made for each of the three cations, Sm^{3+}, Bi^{3+} and Fe^{3+}. All three were made by dissolving $Sm(NO_3)_3 * 6H_2O$ (Sigma Aldrich 99.9%), $Bi(NO_3)_3 * 5H_2O$ (Fluka >98%) and $Fe(NO_3)_3, * 9H_2O$ (Sigma Aldrich >98%) respectively, in distilled water by use of HNO_3 (Merck 65%) to decrease pH for an increase of the solubility. For Sm- and Fe-solutions, the target pH was ∼1.5 and for Bi-solution between 0 and 1. The solutions were put on a magnetic stirrer and heated to ∼100°C for 24h. Then 2-3mL of each solution were added to preheated porcelain crucibles with kaoline wool where both crucible with wool and the solution in them was weighted. The Sm and Fe solutions were heated to 800°C and the Bi solution was heated to 600°C, due to the volatility of bismuth. A heating rate of 50°C/h was chosen to prevent boiling and thus possible loss of material in the process. After the calcination, the resident material was weighted together with the crucible. All the heat-treatment were done in four parallels to increase the accuracy of the standardization. At last the average concentration and standard deviations of each parallel were calculated.

3.1.2 Pechini synthesis

Either tartaric acid (Acros Organics 99.5%) or citric acid (Acros Organics >99%) were dissolved in distilled water in two pyrex beakers and heated to 50°C over a magnetic stirrer. Accurate amounts of Bi-nitrate, Fe-nitrate and Sm-nitrate precursor solutions were mixed in a pyrex beaker and mixed over a magnetic stirrer. The diluted carboxylic acid was added to the Bi/Fe-nitrate solutions, and to some syntheses, ∼2.5mL of ethylene glycol (Arcos Organics 99.9%) were added. After a few minutes of stirring to ensure there was no visible precipitation, the final solutions were poured into crystallization jars and heated to 100°C or 130°C for 20h. The synthesis route is illustrated in Appendix A.

In this project, a total of 15 syntheses were done, varying the following parameters to achieve a product as phase-pure as possibe:

- Concentration of cation solutions.

- Complexing acid (tartaric or citric).

- Amount of complexing acid (mol fraction to cation solutions).

- pH of solution (regulated by addition of HNO_3).

- Eventual addition of ethylene glycol (EG) as a complexing agent.

- Temperature of hot plate for evaporation.

An overwiew of the synthesis parameters for the relevant syntheses are presented in table form in Appendix C.

Because there were problems with secondary phases though all syntheses, a test synthesis was done using only 75% of the original bismuth precursor solution to investigate how this eventually affected the bismuth-rich secondary phase or phases.

35

3.1.3 Calcination

Prior to calcination the synthesis products were ground in a mortar to achieve a soft and small grained powder and stored in small sealed glass containers. Calcination were done using porcelain crucibles in normal atmosphere in a range of temperatures from $300^{o}C$ to $600^{o}C$, holding for 2h and with a heating rate of $100^{o}C/h$. The calcination scheme is given in figure 18. Some crucibles were weighted before and after calcination to estimate eventual mass losses.
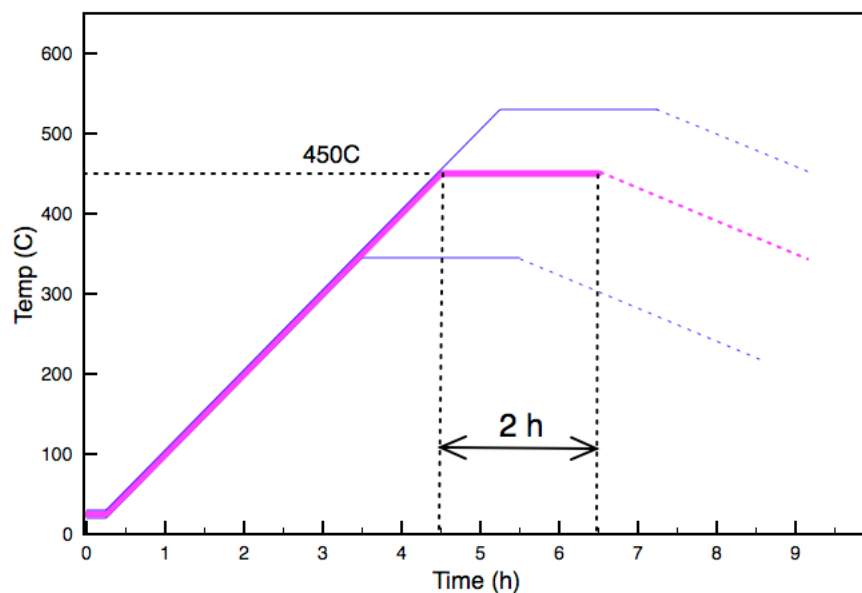

Figure 18: Calcination scheme for $450^{o}C$ calcination for 2h. Calcination schemes for $350^{o}C$ and $525^{o}C$ in blue for comparison.

3.1.4 Sintering

Some powders were prepared for sintering by ball milling in ethanol with 3mm yttrium-stabilized zirconia balls for 2h followed by Rotavapor drying. The milled powders were pressed in an uniaxial press at 50MPa, 100MPa, 150MPa, 200Mpa and 250MPa using a 10mm circular tool.

A range of sintering tests were carried out on 100MPa pressed pellets to find the optimal sintering temperature; 875°C, 900°C and 925°C. The sintering were done for 15 minutes on an alumina plate and covered on all sides with precalcined $Bi_{0.9}Sm_{0.1}FeO_3$ powder. For the final sintering, a pressure of 200MPa and a sintering temperature of 875°C was chosen from the results of the testing. A caliper and weight method described in Appendix E and Archimedes method [52] were used to measure pellet density.

3.1.5 Sample preparation

After sintering, the pellets were prepared for measurements by wet-polishing with 800 grains/in^2 and further with 4000 grains/in^2. After polishing, the samples were examined using an optical microscope. Gold electrodes for electrical measurements were sputtered on each side of the pellet using an Edwards Sputter Coater S150B while the circumference of the pellet was masked with adhesive tape. The sputtering were monitored visually and halted when the gold layer were clearly covering the surface. A figure illustrating the geometry of the samples is presented in chapter 4.

3.2 Characterization

3.2.1 X-ray diffraction (XRD)

All syntheses were examined by a quick XRD run, using a Bruker D8 Focus with 2θ angles from 10 to 80 with 0.02 degrees step size and a fixed slit of 0.2mm. The count time per step were 0.2 seconds. These tests were done to get a rough overview of the phase composition to decide if a synthesis product was to be used or considered defective.

For the selected syntheses, uncalcined powder and calcined powders were run using the same XRD setup as described above, except the count time. For these runs, the count time were either 1 seconds per step (synthesis 3 and 4) and 4 seconds per step (synthesis 12).

For the sintered pellets, XRD were run using the identical parameters as for synthesis 3 and 4.

3.2.2 Rietveld refinement

For Rietveld [53] refinement of XRD data, software Topas Bruker R (Bruker AXS) version 4.2 was used. A hkl-inputfile for the perovskite was used to identify the perovskite phase, and eventual other phases were marked manually. Background and sample displacement were corrected for, and all refinements were done until the desired variables converged satisfactory. From the refinement, hexagonal unit cell parameters were calculated for all calcined temperatures of synthesis 12. Full-width-at-full-maximum (FWHM) [36] crystallite sizes were also calculated. In addition, cation positions for Bi^{3+}/ Sm^{3+} and Fe^{3+} were refined for the same powders.

3.2.3 Calorimetry (DSC)

Diffential scanning calorimetry (DSC) [54] experiments were run to investigate phase transformations yielding the Neel temperature, T_N, and Curie temperature, T_C. A change in the heat transfer to and from the sample indicates a change in the material, such as a phase change [54]. Selected samples of 25-35mg were run using a Perkin Elmer DSC7, heating from 25^oC to 425^oC at 40K/min, holding for 1 minute and cooling back to 25^oC at the same rate. Some samples were run using the same machine and variables, but increasing the heating rate to 550^oC to identify the Curie temperature. An identical DSC experiement at 10K/min were done to complement the other measurements. Two samples were also run using a Netzsch STA 449C Jupiter in two loops at 40K/min from 25^oC up to 850^oC. Table 3 lists the varied parameters and the powders used for DSC measurements.

$T_{calcination}$ (C)	Perkin Elmer	Netzsch	DSC T_{max}(C)	Expected results
450	X		450	T_N
450		X	850	T_C
475	X		450	T_N
500	X		450	T_N
500	X		550	T_C
500		X	850	T_C
525	X		450	T_N
550	X		450	T_N
600	X		450	T_N
850	X		450	T_N
850	X		550	T_C
850	X		550 (10K/min)	T_C

Table 3: Overview of DSC experiments. All powders were from synthesis 12, starting at 25^oC and heating by 40K/min if not otherwise noted.

3.2.4 Electrical measurements

Prepared sintered pellets were tested using an aixACCT piezomeasurement system. Parameters that were changed are:

- Signal amplitudes from 100 V/mm to 3 kV/mm

- Signal frequencies from 0.001 Hz to 1 kHz, triangular waveform

- Sample chamber temperature at 25^oC (room temperature) and 100^oC

All pellets were covered in nonconductive oil to prevent discharge between electrodes in the sample chamber. All pellets were also checked for contamination of gold or other materials around their edges to prevent electrical shorts or defects.

From the measurements, polarization, current and mechanical displacement data were obtained.

.

4 Results

4.1 Synthesis and preparation

4.1.1 Pechini syntheses

As described in chapter 3, all syntheses were tested by a quick XRD run for both calcined and uncalcined powders. None of the synthesis products were phase pure, but some were far better than others. The dominant secondary phase is bismuth oxide, Bi_2O_3 or a similar composition (e.g. sillenite, $Bi_{25}FeO_{39}$ /$Bi_{25}FeO_{40}$). The syntheses containing the least amount of secondary phases were the ones selected for further experiments (synthesis 1, 3, 4 and 12).

Synthesis 16, a test synthesis to test if there were a stochiometry error from the standardization results, also contained the same secondary phases, although in a slightly smaller amount. This phase does however nearly disappear at higher calcination temperatures for all syntheses, appearent in figure 21 and 22.

4.1.2 Powder preparation and sintering

A visual check on the ball milled powders showed that the powders had little or no soft agglomerates and after pressing, and the densities of green body pellets were in the 40-60% range, plotted in figure 19. The surfaces were clean with no visible cracks or chips. Table 4 gives an overview of the density for the sintered samples measured by caliper and weight and the Archimedes method, in addition to mass loss and volume shrinkage.

Powder	Pressure	Sint. temp	Mass loss	Vol. shrink	Caliper	Archimedes
Synt. 1	100 MPa	875^oC	1.78 %	52 %	97.5 %	-
		900^oC	1.72 %	49.7 %	95.2 %	-
		925^oC	1.77%	51.5 %	99.1 %	-
Mixed synt.	100 MPa	875^oC	-	-	72.7%	-
	150 MPa		-	-	76.3%	-
	200 MPa		-	-	80.9%	-
Synt. 3	200MPa	875^oC	0.31%	-	93 %	95.1 %
			0.32%	-	91 %	95.3 %

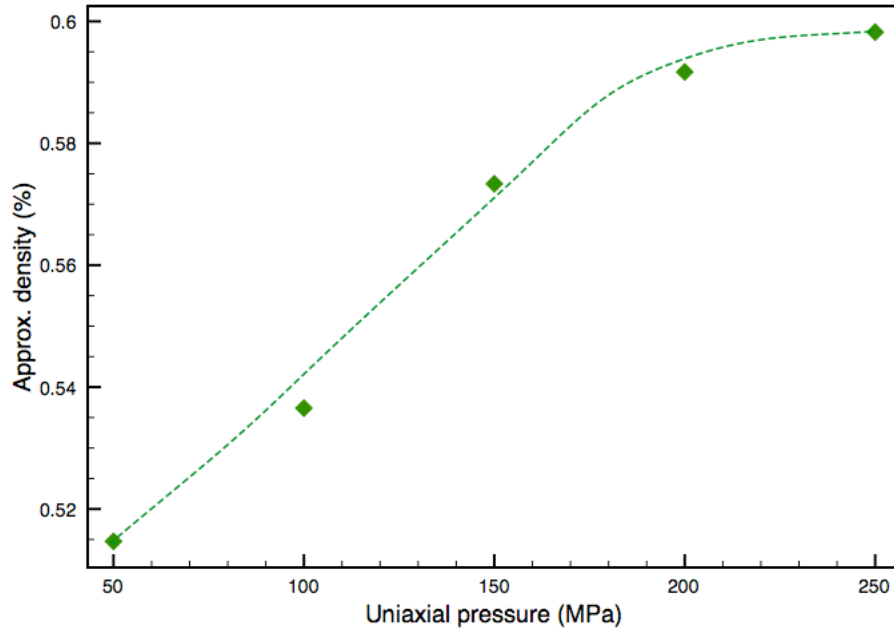Table 4: Density, mass loss and volume shrinkage for sintered pellets.

Figure 19: Green body density (caliper method) as function of applied uniaxial pressure.
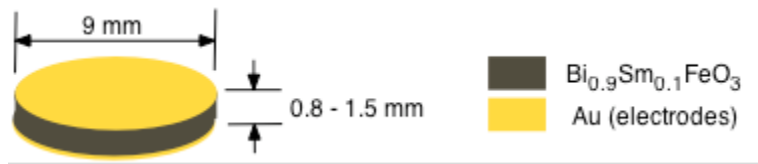

Figure 20: Illustration of the geometry of sintered pellets with gold electrodes. Actual dimensions are given.

4.2 Composition and crystal structure

4.2.1 X-ray diffraction

XRD diffractograms for green bodies and sintered pellets for the two powders used are presented in figure 21. Note the sillenite peak for the green bodies of mixed powders at $2\theta = 28^o$
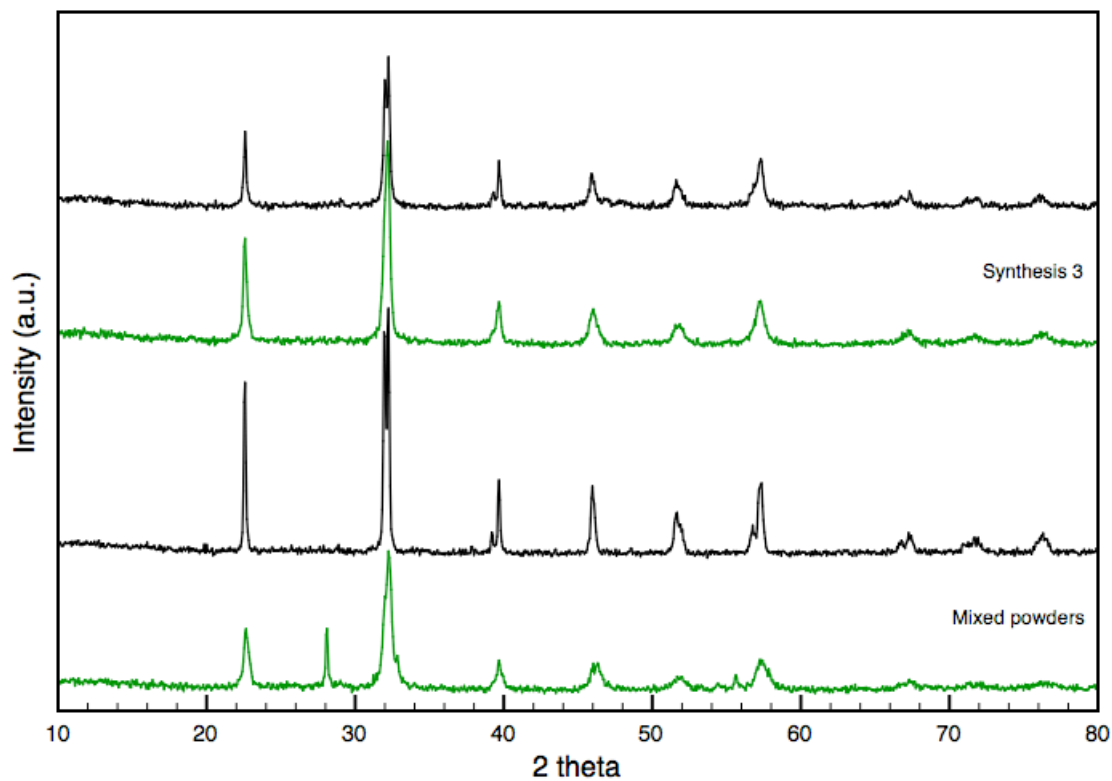

Figure 21: XRD raw data for green body (green plots) and sintered pellets (black plots).

The complete X-ray diffraction data from synthesis 12 is given in figure 22 (next page), marked with the calcination temperatures. Derived data are presented in the next section.
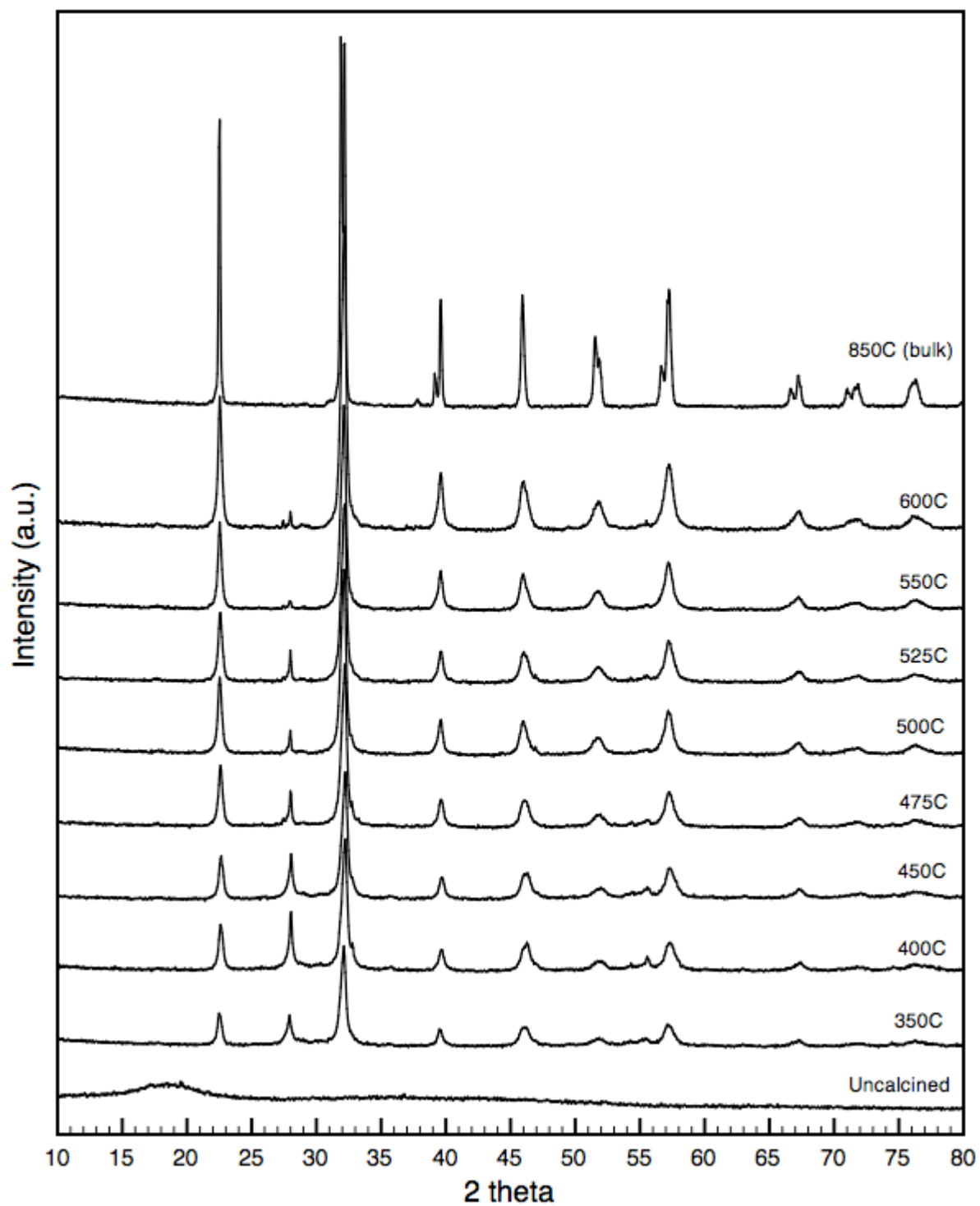
Figure 22: XRD raw data from syntesis 12.

4.2.2 Rietveld refinement

Calculated crystallite sizes (FWHM) and refined unit cell parameters for synthesis 12 are given in table 5, and plotted in figures 23 and 24.

Calc. temp	Cry.size (nm)	a_{hex} (Å)	c_{hex} (Å)	a_{norm} (Å)	c_{norm} (Å)	c_{norm} / a_{norm}
350ºC	21.068	5.5554948	13.6873862	3.928328046	3.951208054	1.00582436
400ºC	21.238	5.5493493	13.6791206	3.92398252	3.94882198	1.00633017
450ºC	21.071	5.5555444	13.6903654	3.92836312	3.95206807	1.00603431
475ºC	22.837	5.5663878	13.7513484	3.93603056	3.96967235	1.00854714
500ºC	25.360	5.5726658	13.7867232	3.94046978	3.97988418	1.01000246
525ºC	26.508	5.5744765	13.7918070	3.94175013	3.98135174	1.01004671
550ºC	28.677	5.5748137	13.7944868	3.94198857	3.98212533	1.01018186
600ºC	29.997	5.5768785	13.7958021	3.94344861	3.98250503	1.00990413
850ºC	89.389	5.5763927	13.8022520	3.94310509	3.98436695	1.01046431

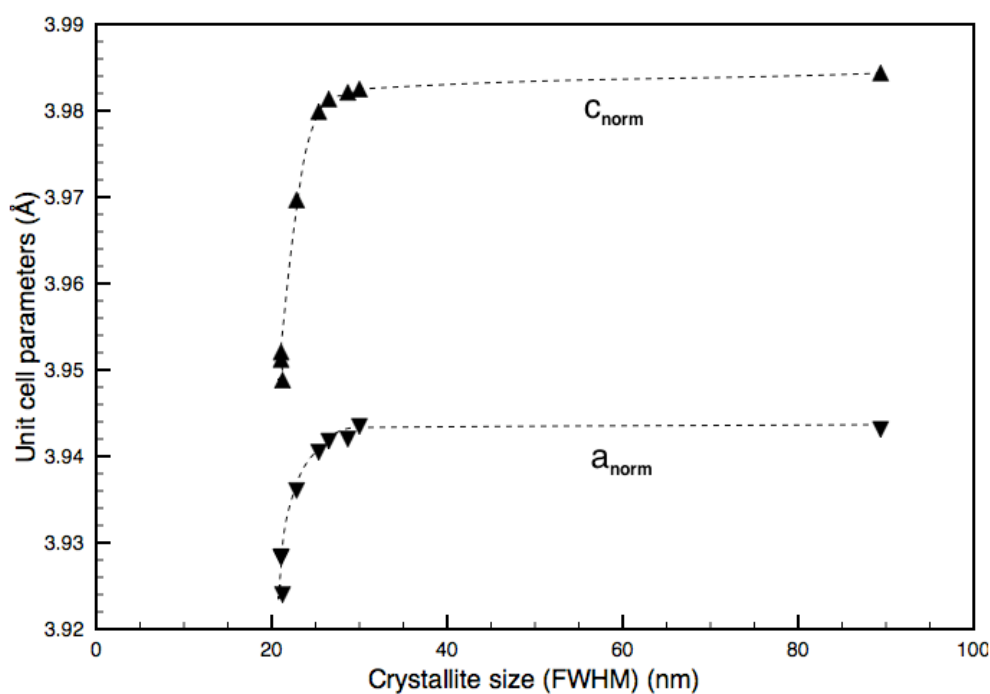Table 5: Crystallite sizes (FWHM) and refined unit cell parameters.

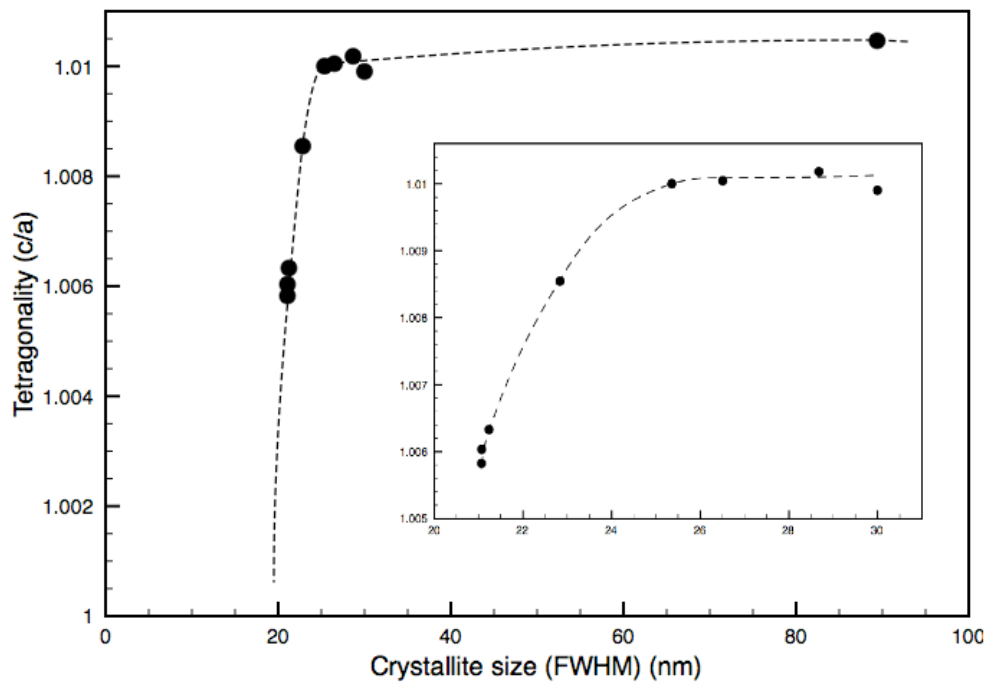Figure 23: Normalized unit cell parameters as function of crystallite size with trendlines.

45

Figure 24: Tetragonality factor (c_{norm} / a_{norm}) as function of crystallite size with trendline. Insert is zoomed view of nanocrystalline data points.

The refined cooperative displacements for Bi^{3+}/ Sm^{3+} and Fe^{3+} cations are plotted in figure 25 as a function of refined crystallite size.
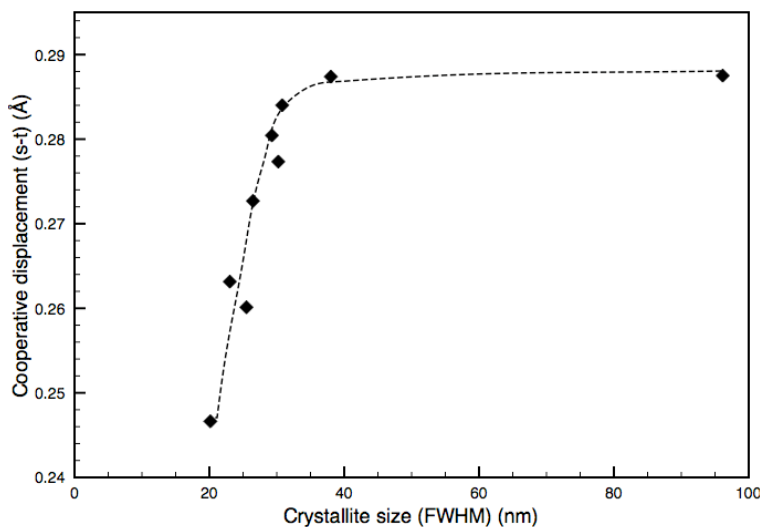

Figure 25: Cooperative displacement s-t as function of crystallite size with trendline.

4.2.3 Calorimetry

Plots of the phase transitions found from the last (third) loop of DSC results are presented in figures 26 and 27.
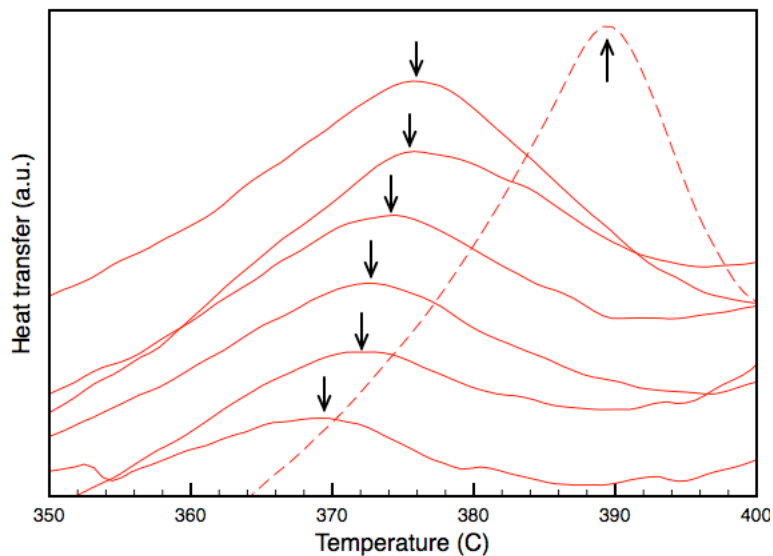

Figure 26: Heat flow changes in heating data from Perkin Elmer DSC7 (endo up). Dashed line is bulk powder. Midpoint of each transitions is marked with an arrow.
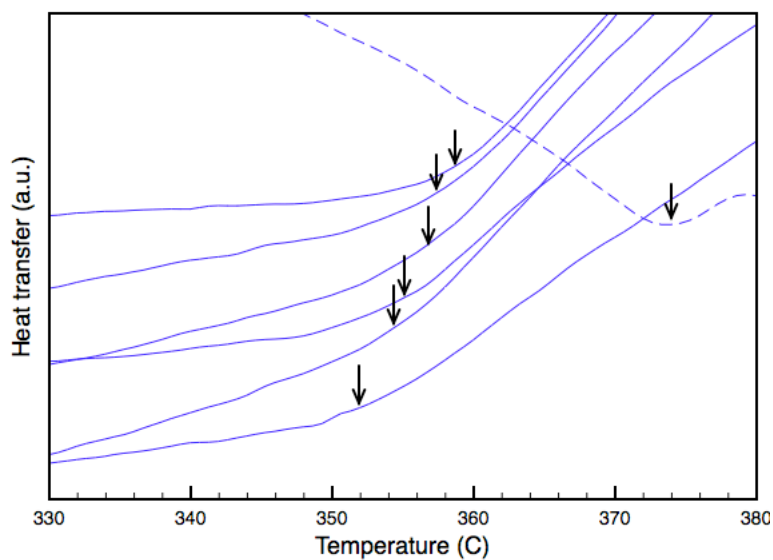

Figure 27: Heat flow changes in cooling data from Perkin Elmer DSC7 (endo up). Dashed line is bulk powder. Midpoint of each transitions is marked with an arrow.

The data collected from the two-loop DSC runs up to 850°C is presented in figures 28 and 29.
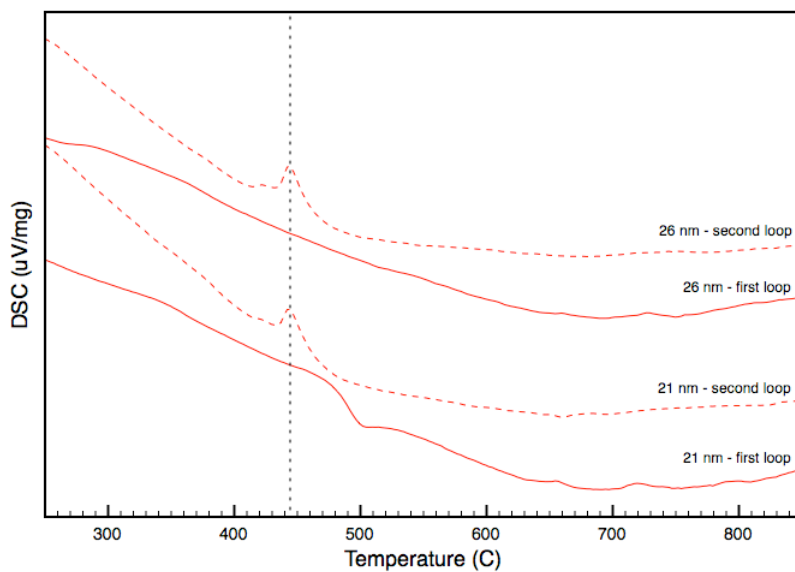

Figure 28: DSC data up for heating (endo up). The solid lines are for nanocrystallites, while the dashed lines are for the same powders in their second loop (bulk).
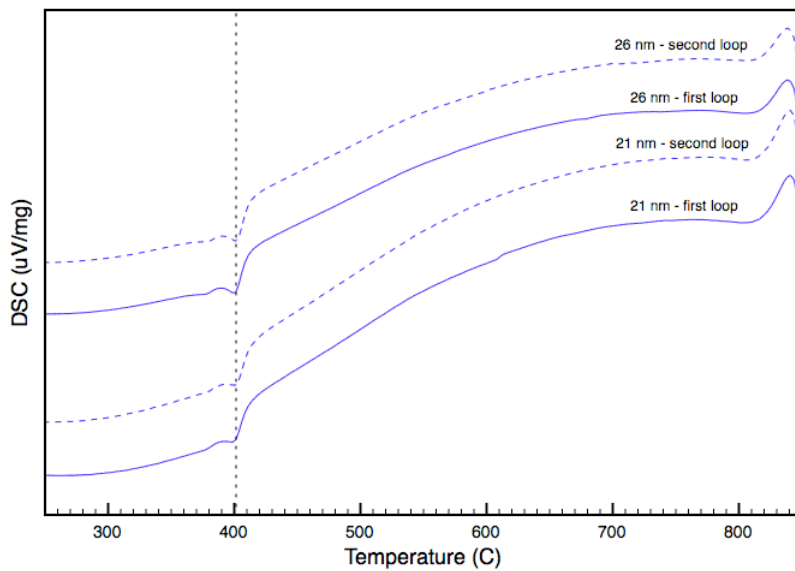

Figure 29: DSC data up for cooling (endo up). The solid lines are for nanocrystallites, while the dashed lines are for the same powders in their second loop (bulk).

4.3 Ferro- and piezoelectric properties

From all the measurements done at all different parameter settings, the samples were too conductive to get any polarization or displacement data. At signal amplitudes higher than $\sim 1.5 \text{kV/mm}$, the maximum current for the test equipment were reached for even the least conductive samples. Calculations on the current-voltage plots give a resistance of the samples in the 10 kΩ/mm to 50 kΩ/mm range. Typical current-voltage relationships for the pellets tested are presented in figures 30 and 31.
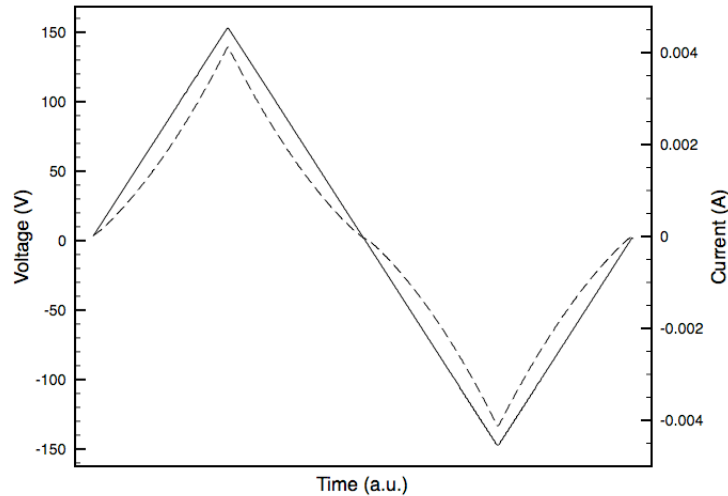

Figure 30: Current-voltage characteristics of conductive pellet. Solid line is voltage over 1mm sample, dashed line is current trough it.

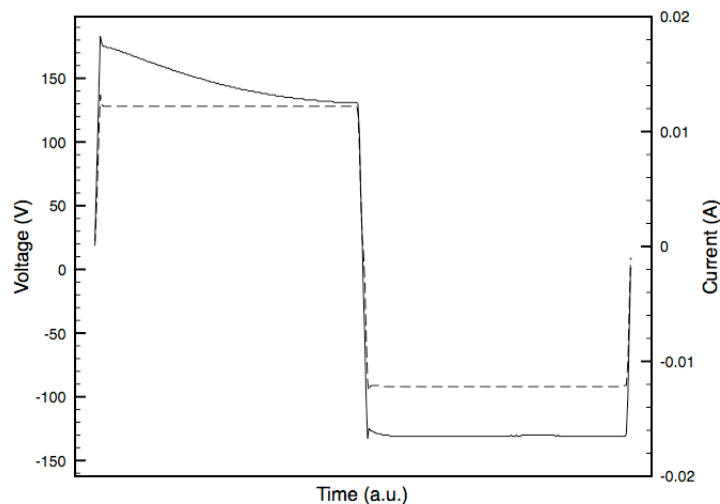
Figure 31: Current-voltage characteristics of conductive pellet showing the current limiation system of the instrument restricts the voltage due to too high conductivity. Solid line is voltage over 1mm sample, dashed line is current trough it.

.

5 Discussion

5.1 Synthesis

Secondary phases The main secondary phase, appearent at 2θ=28 degrees, is according to the PDF database (JCPDS 86-1518), sillenite $Bi_{25}FeO_{39}/Bi_{25}FeO_{40}$, also reported by many other groups [1, 59, 61, 62]. From Appendix C, it is appearent that neither drying temperature, excess of carboxylic acid or addition of ethylene glycol affected the secondary phases appearent after calcination at temperatures below 550^oC. However, lowering the pH solved the issues of visible early precipitation from solution, beeing the main measurable difference between synthesis 3 and synthesis 12. This precipitation is probably visible in the XRD plots as an amorphous background between 2θ from approximately 25 to 35. This is illustrated for synthesis 3 in figure 32.

The choice of complexing acid, tartaric or citric, also made no clear difference regarding secondary phases. This is also illustrated in figure 32, where synthesis 4 is using citric acid, the other two tartaric. However, the synthesis products when using citric acid were not completely dried, even after tripling the time on the heating plate to 60h, still yielding an oily and sticky consistence. The reason for this may be the different nature of the acids and their possible reaction with other species in solution such as ethylene glycol. After calcination at 300^oC or higher, the powders were completely dry.

Summarizing, none of the variables had significant influence on phase purity, and no experiments managed to defeat the formation of the sillenite phase. At that point, there are two main suggestions that may explain the formation of such phase; 1) a global stochiometry error or a 2) thermodynamics problem in the solution.
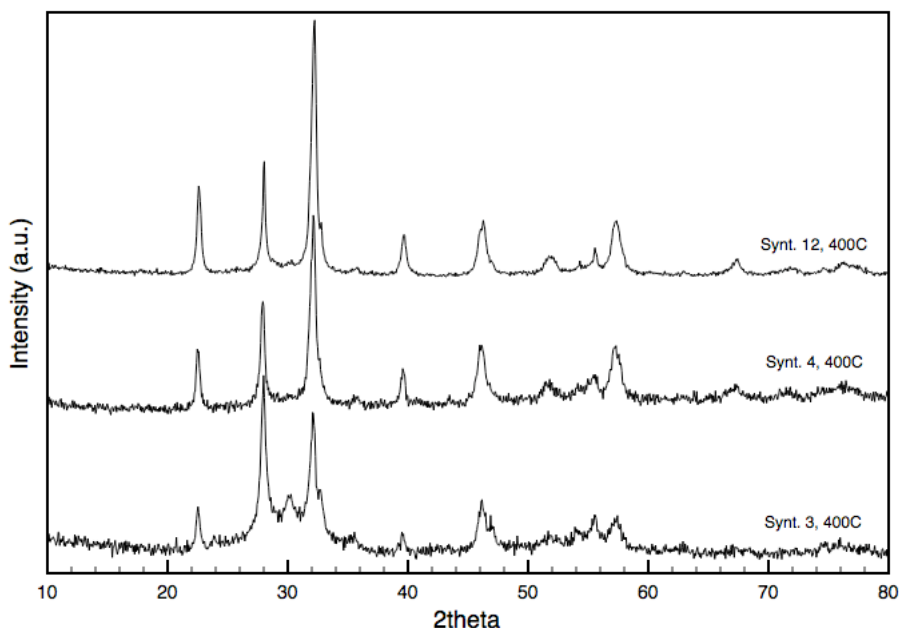

Figure 32: Comparison of synthesis 3, 4 and 12.

Stochiometry test synthesis The results from the stochiometry test synthesis with 25% less Bi^{3+} cations showed the same trend as all the other syntheses, presented in figure 33, making the possibility of a global non-stochiometry in solution, which creates a surplus of bismuth, unlikely. This fact points in the direction of a kinetics problem in solution, facilitating formation of unwanted phases in a specific range of calcination temperatures.
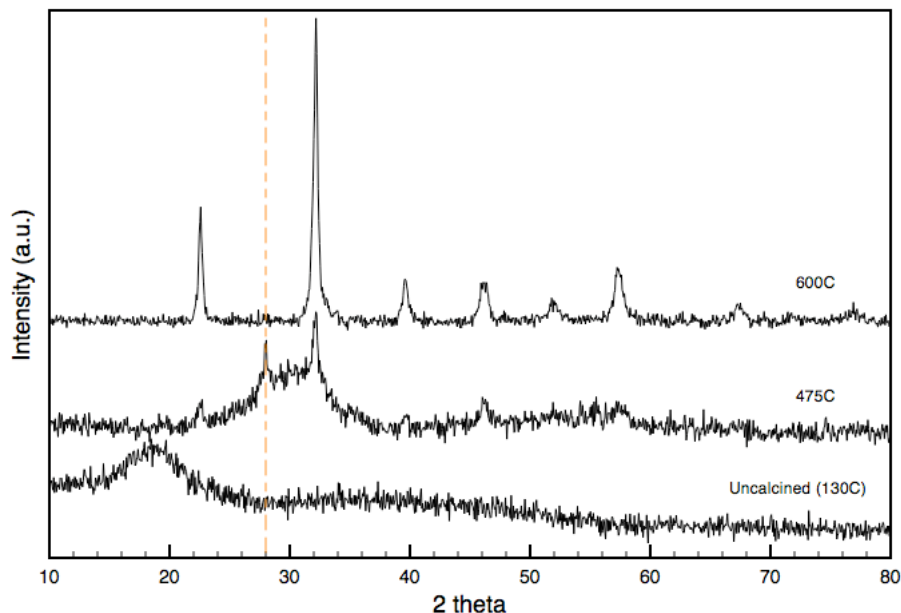

Figure 33: Test synthesis (synthesis 16) results, showing the trend of sillenite appearence at $2\theta = 28^o$, in this case for the 475^oC calcined powder. The dashed line is a guide to the eye.

At lower calcination temperatures, kinetic effects will dominate the structure in the powder, while at higher temperatures, the mobility of the species increase, and equilibrium will eventually be reached if a high enough thermal energy is applied at a sufficient amount of time. If there is correct stochiometry in the material, the thermodynamically favoured phase will be formed at equilibrium conditions. If then the favoured phase the experiments are assumed to be the perovskite, which according to reports it is [22], equilibrium is reached in the powders heated to 600^oC or higher. However, the equilibrium composition found here may not be the equilibrium composition at higher temperatures or pressures [1].

Crystallite size distribution The reason for the range of calcination temperatures is to achieve a range of crystallite sizes to investigate size effects from. It is therfore important that that initial nucleation from amorphous material yields as small crystallites as possible. The different syntheses differs substantially at this point. Synthesis 3 started at ∼13nm, synthesis 4 started at ∼15nm, while synthesis 12 started at 21nm crystallites. The reason why synthesis 12 was chosen is the fact that it was more phase-pure than the others, and the fact that it yielded a larger amount of powder, needed for high-quality XRD diffraction. The size distribution of synthesis 12 was according to table 5 in the 21-35nm range, in addition to the bulk sample, calculated to contain on average 81nm crystallites. It should be noted that the calculation of crystallite sizes for bulk material is very inaccurate compared to data for nanocrystallites [36].

From figure 22 and table 5, it is noticeable that the 350^oC, 400^oC and 450^oC samples from synthesis 12 all had virtually the same crystallite sizes. This fact points in the direction of either a combustion in the preparation, which may heat the powder to a higher temperature than that of the oven, or, a nucleation issue where crystallites need to be at a certain size to be thermodynamically stable. If there was a combustion process, it must have taken place during calcination, since uncalcined powders were amouphous, with reference to figure 22.

5.1.1 Sintered pellets

The sintering results showed that the density of the pellets were approximately the same using caliper-and-weight and Archimedes methods. During the measurements, the sintered pellets showed to be relatively robust mechanically and no cracking from the sintering process was found, even though the green bodies were pressed at relatively high pressures [4] at up to 250MPa.

As this project was no study of powder preparation and sintering techniques, the milling and sintering processes decribed in this text are not optimized. It should be expected to achieve better densities if optimization is done. The geometry of the milled powder grains are also important for the sintering, and if investigated using appropriate techniques, can aid the sintering of denser pellets [4].

Regarding phase composition in the sintered pellets, it can be observed in figure 21 that even the short time heating at 850^oC during the sintering is sufficient to decompose the sillenite phase, with reference to the diffractograms for green body and sintered pellets of the mixed syntheses.

5.2 Crystal structure

The XRD diffractograms shows that the dominant phase in all powders are the perovskite R3c phase similar to pure $BiFeO_3$, the peak positions and relative intensity matches those of other experiments [1, 59, 60, 62]. The other structures present in the material are the already discussed sillenite phase and probably some small amounts of iron-rich impurity phases, such as mullite, $Bi_2Fe_4O_9$. The decrease of the sillenite phase visible in figure 22 at increasing calcination temperature and crystallite size is by all means an effect of the higher temperature, and not a size effect. The sillenite phase is assumed to have no impact on perovskite phase crystal structure [1]. There has not been found any changes in the perovskite structure alongside the decrease of the sillenite phase, a fact that supports the structure independency assumption.

Decrease of the c parameter has been found to decrease with decreasing crystallite size in experiments by Selbach [1], in compliance with data shown in figure 23. However, the data for the a parameter in figure 23 does not comply with Selbachs results, for which the a parameter is increasing upon a decrease in crystallite size. Results from $Bi_{0.9}La_{0.1}FeO_3$ by Hatling [2] reports the a parameter as stable at least down to 20nm crystallite size. This gives an interesting trend, qualitatively illustrated in figure 34. Nevertheless, results by Shetty et. al. [45] states the a parameter as decreasing as a finite size effect on $BiFeO_3$, contradictory to this statement.
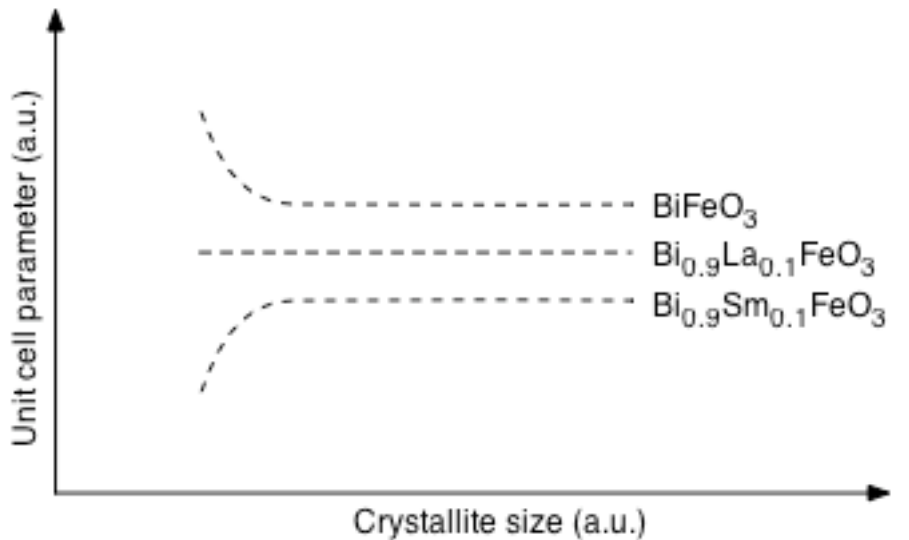

Figure 34: Qualitative illustration of finite size effect on a unit cell parameter as function of rare-earth substitution.

Based on the discussion above, the unit cell volume behavior as a function of decreasing crystallite size differs for $BiFeO_3$, $Bi_{0.9}La_{0.1}FeO_3$ and $Bi_{0.9}Sm_{0.1}FeO_3$ compositions. The cell volume is plotted for these three in figure 35.
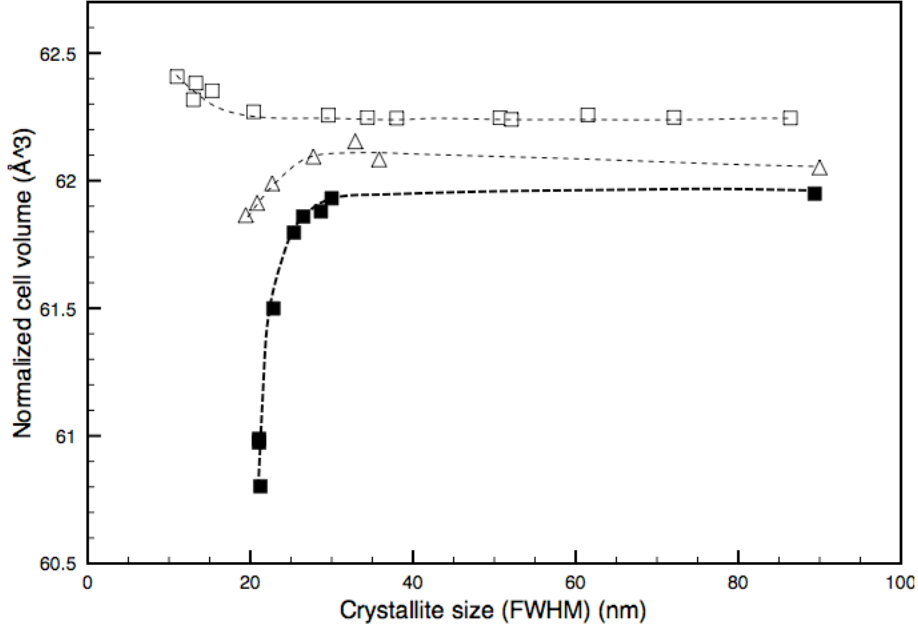
Figure 35: Comparison of unit cell volume between this experiment (filled squares, bold trend-line), data for unsubstituted $BiFeO_3$ by Selbach [1](open squares) and data for $Bi_{0.9}La_{0.1}FeO_3$ by Hatling [2] (open triangles).

From figure 24, it is clear that the tetragonality of the unit cell decreases from the c_{norm} / a_{norm} = 1.01 value for bulk material. For crystallite sizes of 21nm, this value is at 1.006, and extrapolation of the trend predicts a halving of this value at ~20nm. Cubic structure, c_{norm} / a_{norm} = 1, will from the same interpolation be reached at sizes slightly below 20nm. It must be noted that the crystallite sizes calculated in this experiment can not be directly compared to other experiments, as there are differences in how the sizes are calculated. However, comparing data within the same experiments are possible when the same method and settings are used for all calculations, as it is in this case. The calculation variations make the comparison to experimental data by Selbach [1] and Hatling [2] along the size axis inaccurate, but there is a trend for the extrapolation of the tetragonality trendlines for the three compositions to the size where c_{norm} / a_{norm} = 1, d_{cubic}: d_{cubic}(Sm-substituted) > d_{cubic}(La-substituted) > d_{cubic}(unsubstituted).
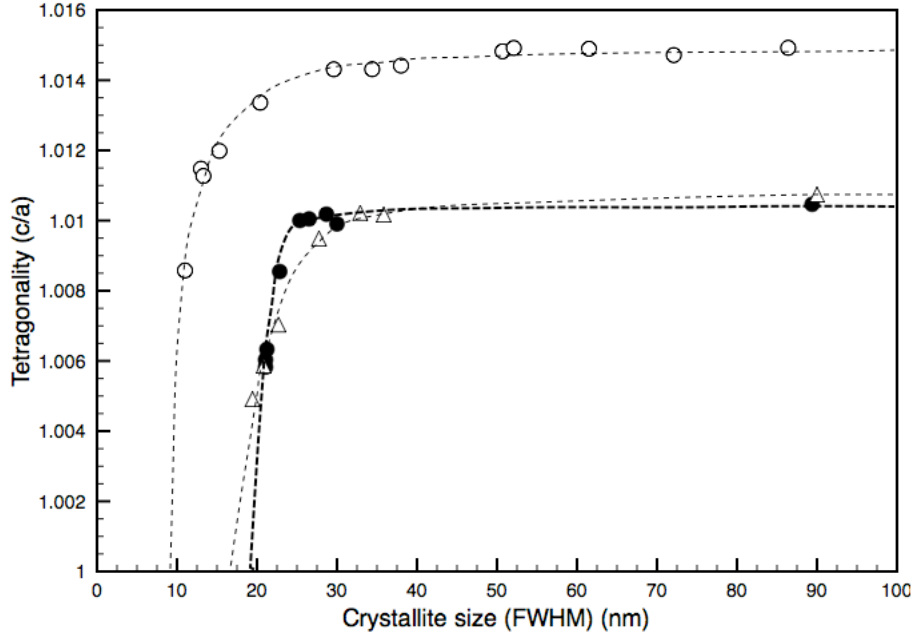
Figure 36: Comparison of unit cell tetragonality between this experiment (filled dots, bold trendline), data for unsubstituted $BiFeO_3$ by Selbach [1](open circles) and data for $Bi_{0.9}La_{0.1}FeO_3$ by Hatling [2] (open triangles).

Another interesting fact to observe from figure 36 is the decrease in the bulk tetragonality upon a decrease in substituted cation size. This is believed to originate from the fact that the Sm^{3+} cation does not posess $6s^2$ lone-pair electrons that Bi^{3+} does. This will therefore partially destabilize the asymmetric ferroelectric structure compared to pure $BiFeO_3$. This proposal is in coincidense with the data presented in figure 36, where c/a values for $Bi_{0.9}Sm_{0.1}FeO_3$ and $Bi_{0.9}La_{0.1}FeO_3$ is similar, and differs clearly from the value for $BiFeO_3$.

Due to the tetragonality present for all powders from the synthesis, separate peaks for the two different unit cell vectors a_{hex} and c_{hex} are expected but not visible in most of the diffractograms since the small crystallite sizes results in peak overlap. However, for samples calcinated at 850^oC and for the sintered pellets, peak splitting are visible, with reference to figure 21 and figure 22. Unit cell tetragonality is an important measure of the electrical properties of the material, which will be discussed in the next chapter.

5.3 Electric properties

5.3.1 Cation displacement

A decrease in the s-t parameter is probably due to weaker ferroelectricity, and could in turn increase the piezoelectric response due to a reduced switching threshold. As the tetragonality factor c/a decreases, a decrease in s-t could therefore be correlated, since the increased tetragonality of the unit cell increases the remanent polarization. Compared with data for pure $BiFeO_3$, provided by Selbach [1], it is clear that the bulk value for the cooperative displacement is $\sim 36\%$ higer than for the samarium substituted composition. According to Hatling, cooperative displacements for $Bi_{0.9}La_{0.1}FeO_3$ also has a bulk value of (s-t) ≈ 0.27Å [2].

Between $Bi_{0.9}Sm_{0.1}FeO_3$ and $BiFeO_3$ there are two main structural differences relevant for polarization; 1) The $6s^2$ lone-pair electrons present in Bi^{3+} but not in Sm^{3+}, and 2) the difference in ionic radii. How these two factors affect the cooperative displacement is not possible to decide from the comparison in figure 37. However, taking data for $Bi_{0.9}La_{0.1}FeO_3$ provided by Hatling [2] into consideration, it looks like the loss of $6s^2$ lone-pair electrons provides the main effect on (s-t), since the lanthanum cation , La^{3+}, like Sm^{3+} does not provide lone-pair electrons. The ionic radii of La^{3+} and Bi^{3+} are close compared to Sm^{3+}, and since the (s-t) values for samarium-substituted and lanthanum-substituted $BiFeO_3$ are within the same range, the cation radii effect is minor in this comparison.
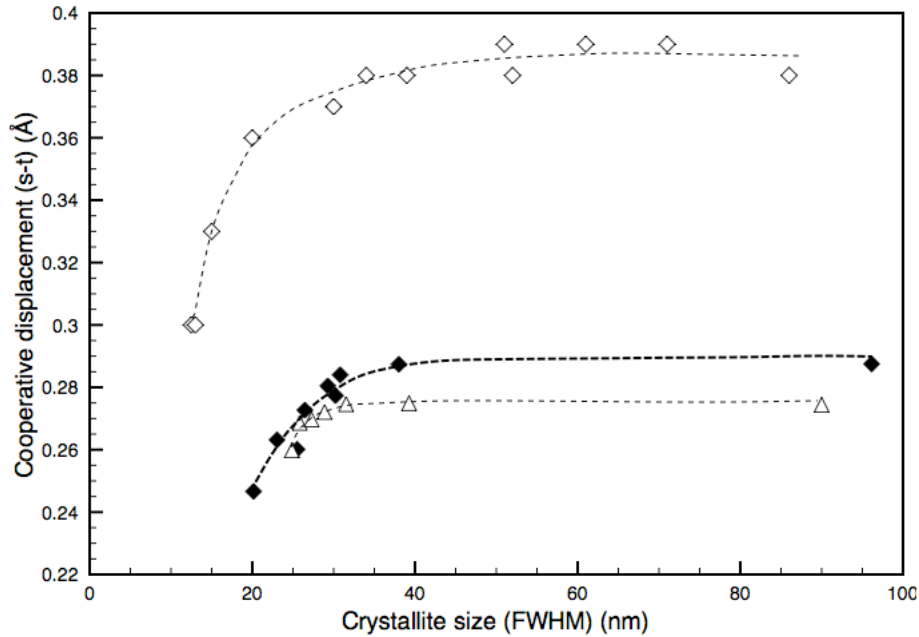

Figure 37: Cooperative displacement s-t from this experiment (filled diamonds, bold trendline) compeared with data for unsubstituted $BiFeO_3$ by Selbach [1] (open diamonds) and data for $Bi_{0.9}La_{0.1}FeO_3$ by Hatling [2] (open triangles).

The relationship between unit cell tetragonality and cooperative displacement is plotted below:
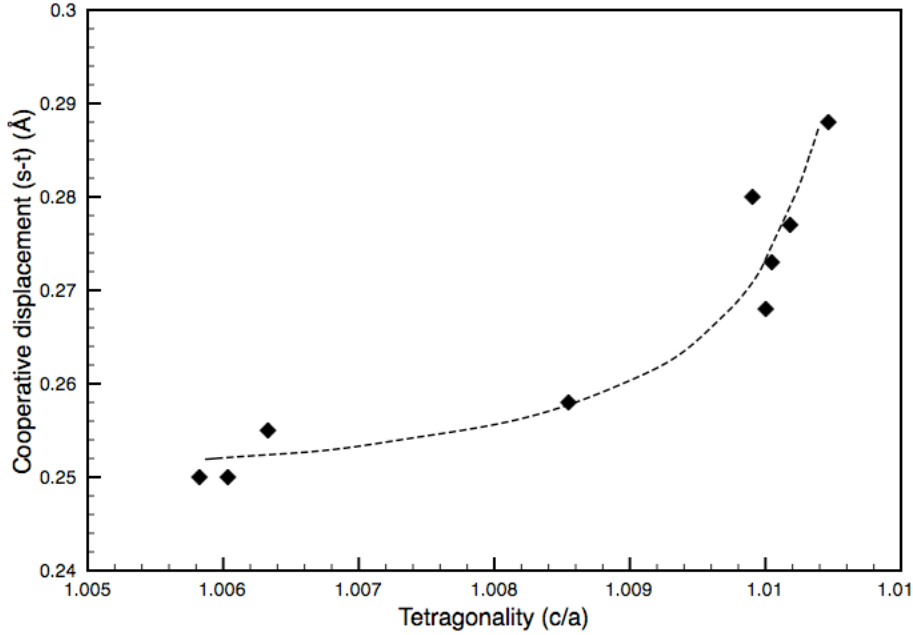

Figure 38: Correlation between tetragonality (c_{norm} / a_{norm}) and cooperative displacement (s-t).

The relationship in figure 38 shows how the polarization represented by the cooperative displacement decreases as a finite size effect at larger crystallites than for which the finite size effect on tetragonality appears. This fact is probably due to the loss of long-range electrostatic forces in the nanocrystallites, which will destabilize polarization. It is from this fact also clear that the decrease in tetragonality is not the main restriction factor for ferroelectric polarization in nanocrystallites, since the polarization decreases while the tetragonality is still constant.

5.3.2 Ferroelectric phase transition

Another important measure [28] for ferroelectric properties is the ferroelectric phase transition at the Curie temperature, T_C. For bulk $BiFeO_3$, $T_C \sim 830^oC$, but when Bi^{3+} is increasingly substituted by a rare-earth cation such as Sm^{3+} or La^{3+}, T_C is expected to decrease, in accordance with results from Karimi et. al. [19]. Another factor expexted to lower the T_C is a decrease in crystallite size, since it it closely coupled to cooperative displacement [1, 28]. Unfortunately, from the DSC data in this experiments, no clear phase transitions can be found for nanocrystallites. A reason for this may be a random polarization orientation at the crystallographic level, yielding only a very small net effect in the sample. When there is diffculty identifying a phase transition from a DSC curve, derivation of the curve to find where the slope changes may be a useful tool, the derivative of the DSC heating runs in the Netzsch instrument is plotted in figure 39.
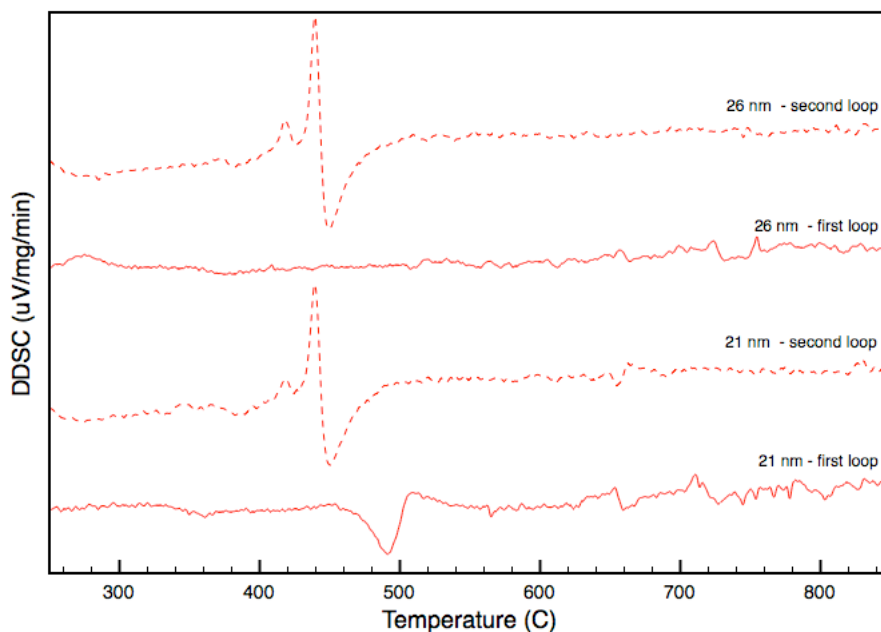
Figure 39: Derivated DSC heating plots (DDSC) from the Netzsch instrument. The solid lines are for nanocrystallites, while the dashed lines are the same powders in their second loop (bulk).

Both from figure 28 and figure 39, a change in the plot at 490^oC-500^oC is clearly visible for the 21nm nanocrystalline powder. This is nevertheless not present in the 26nm nanocrystalline powder and if it was a phase transition, it is exothermic, so it can not be the ferroelectric phase transition but rather be a measurement error in the experiment. The ferroelectric phase transition is as mentioned also expected to be lower for nanocrystallites than for bulk material [19], and even in the derivative plots there are no visible signs of a ferroelectric phase transition.

However, at bulk conditions, after the sample have been heated to 850^oC, clear transitions are found which coincides with the temperature range where T_C is expected to be found [19]. The DSC cooling loops in figure 29 underline this observation, and all cooling loops gives bulk data, since the samples have been heated to 850^oC. The supplementary data from the Perkin Elmer DSC7 experiment also underlines both the heating and cooling data found by the Netzsch instrument. A comparison is given in figure 40.
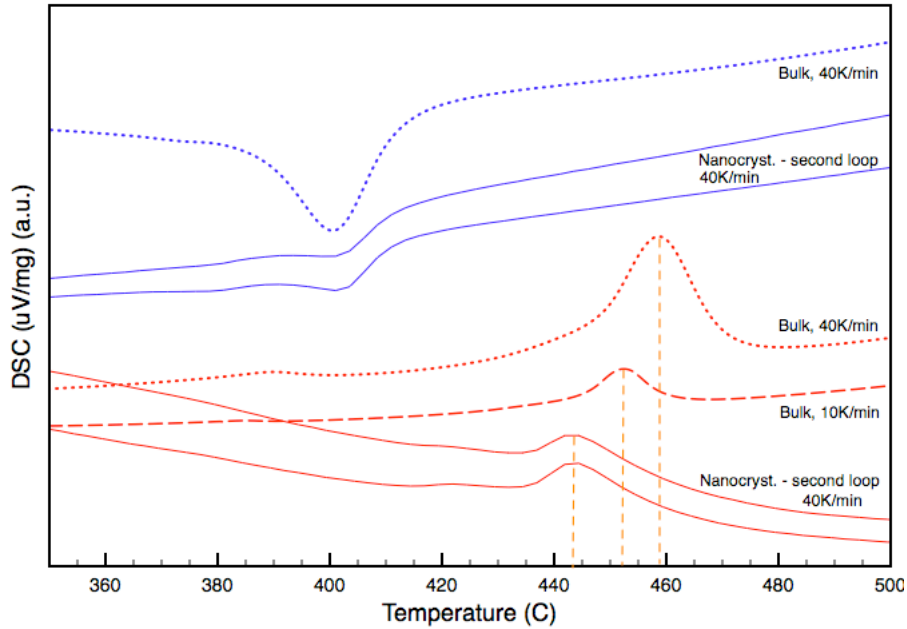
Figure 40: Bulk properties from the two experiments. Red line is heating, blue line is cooling. Solid line plots are done by Netzsch instrument at 40K/min, dashed line plots by Perkin Elmer instrument. Short dashed = 40K/min, long dashed = 10K/min. The horisontal dashed lines are guides to the eye.

From figure 40, it is noticable that there are only a slight variation, within the expected experimental error of a few degrees centigrade, between the two instruments on the cooling portion. However, on the heating half-loop, the difference is 15^oC between 444^oC for the Netzsch and 459^oC for the Perkin Elmer instrument. The same experiment were also run 10K/min, with reference to figure 40. This was done to identify the contribution from the delay in the equipment due to the fast heating rate [54]. From figure 40, it is clear that the deviation between the peaks for 10K/min and 40K/min in the Perkin Elmer instrument is 7^oC, which makes the difference down to 444^oC for the Netzsch intrument still significant. The most evident explanation for this difference is that there is a finite size effect on T_C. However, is is impossible to derive the crystallite size for the curve from the Netzsch instrument. There would have been crystal growth when the samples were heated to 850^oC in the first loop, but from figure 40, it is clear that the crystallite size was well below the one for 850^oC calcined powder. Figure 41 compares this result with data from Karimi et. al. [19]. As always, intrument differences and measurement errors must be taken into account comparing the phase transition peaks.

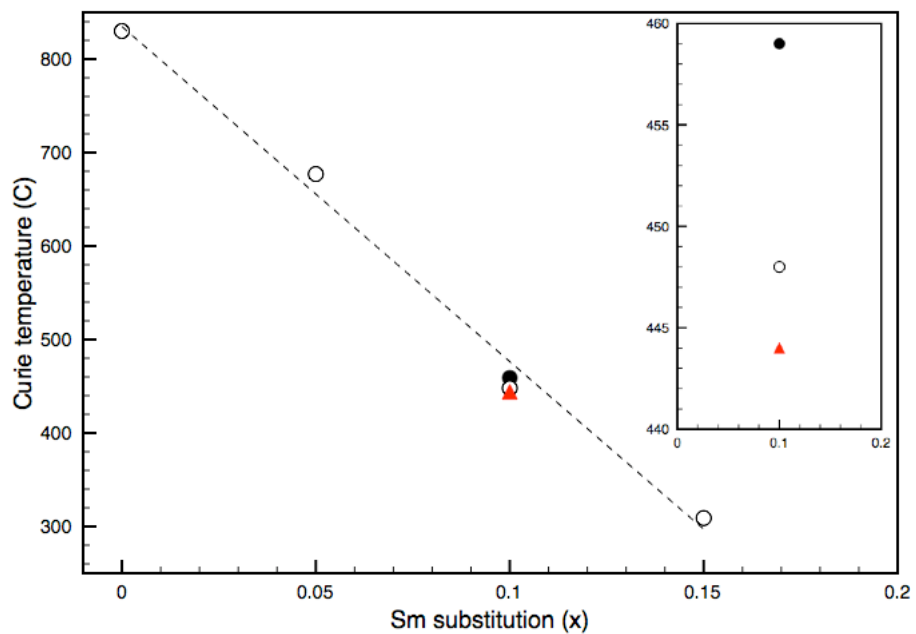Figure 41: T$_C$ as a function of samarium substitution for bulk (black dot) and nanoparticles (red triangle) compared with bulk results from Karimi et. al. [19] (open circles). The inset is a magnified view showing the size effect contribution.

5.3.3 Electrical measurements

All electrical measurements on ferroelectric polarization and piezoelectric displacement were prevented by the too high conductivity of the pellets. An obvious reason for conductivity is deposits by gold or other conductive material from the preparation of the pellets. In this case, ten pellets were tested and all were thoroughly examined for such deposits or electrode defects, and no such were found.

Regarding conductivity in the $Bi_{0.9}Sm_{0.1}FeO_3$ material itself, three suggestions are listed here:

- One or more conductive phases in the bulk material.

- One or more conductive phases at the grain boundaries.

- Impurities or defects on an atomic level along the domain walls.

From the XRD plots in figure 21 it is evident that the amount of phases other than the perovskite phase in sintered pellets is small, if any at all. If the high conductivities that have been found in the measurements were from such phases, they would have been more appearent in the diffractograms. A fact that underscores this is the high X-ray reflectivity of sillenite, due to its high bismuth content, which should make even low concentrations clearly visible in the diffractograms, with respect to diffractograms in figure 32 and figure 33.

Is is an established fact that secondary phases tend to accumulate along grain boundaries in sintered materials [4]. These phases do not mix with the main phase and would therefore fill the gaps between perovskite grains, in this case. Such accumulation may make secondary phase "bridges" through the pellet, effectively connecting the two gold electrodes.

From the synthesis, through characterization and preparation, there are several possibilities of introducing impurities into the material, making electron "jumping" and therefore increase conductivity. Vacancies or other defects in the structure may also have the same effect. From the characterization done in this project, it is not possible to tell that all unit cells are defect-free perovskite, only that the vast majority of them are.

5.4 Magnetic properties

5.4.1 Magnetic phase transition

The only experiments on the magnetic properties were the DSC runs, from which magnetic phase transitions may be identified. As described in chapter 2, the reported Neel temperature of pure bulk $BiFeO_3$ is in the 370-380°C range [1]. Due to the similar magnetic structure of the $Bi_{0.9}Sm_{0.1}FeO_3$ powders used in this experiments, the Neel temperature is expected to be close to the Neel temperature of the pure compound at bulk conditions. Therefore, the measurements were chosen to not exceed 450°C since it probably would not have any effect.

The phase transition curves are plotted above, and resulting temperatures of the paramagnetic phase transitions are plotted in figure 42. There is a clear relation between crystallite size and the phase transition assumed to be the Neel temperature.
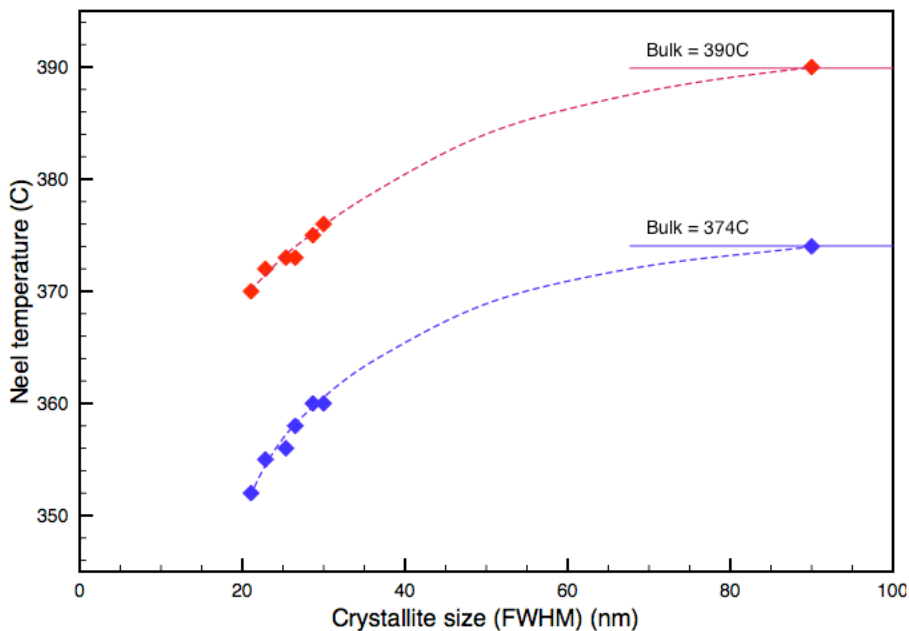

Figure 42: Read-off Neel temperatures from DSC plots. Measured bulk values are included.

The data from the DSC analysis in the Netzsch instrument supports the results presented in figure 42, as the magnetic phase transition is visible, albeit weakly, from the plots at the same temperatures. Consistence between the two intruments inevitably makes the accuracy of the results better.
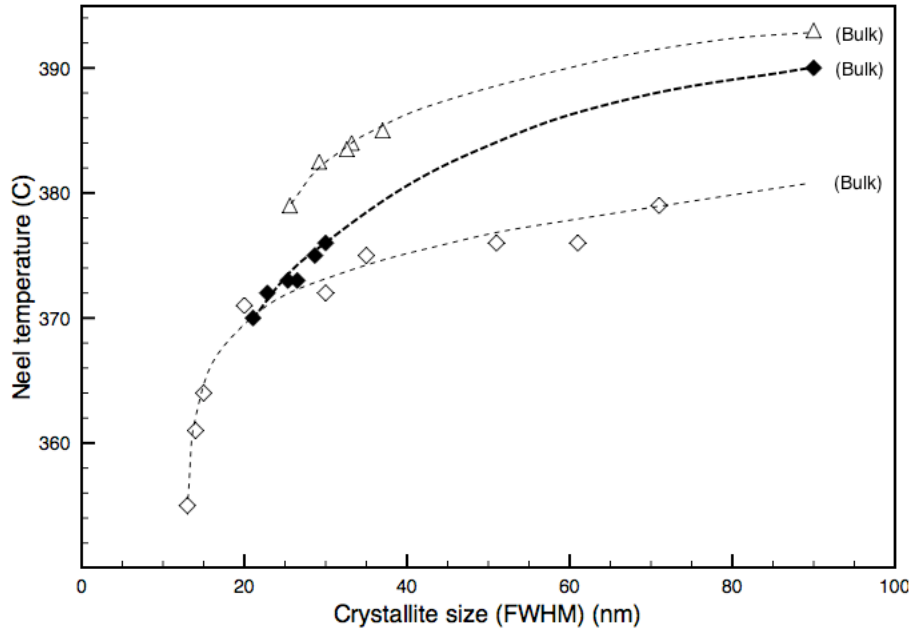
Figure 43: Comparison between Neel temperature for a) This experiment b) Selbach 2009

Comparing the bulk value for the Neel temperature for $Bi_{0.9}Sm_{0.1}FeO_3$ with the bulk value for the pure compound indicates a increase in the paramagnetic phase transition as a result of samarium substitution. The increase of the Neel temperature is in compliance with the stated relationship between T_N and octahedra tilting, which is a result of the substitution by a smaller cation such as samarium, presented in section 2.2.3. The Neel temperature as a function of crystallites size is presented in figure 43 with data for $BiFeO_3$ [1] and $Bi_{0.9}La_{0.1}FeO_3$ [2]. There is a clear trend that rare-earth substitution increases the bulk Neel temperature and all three compositions shows finite size effects.

5.4.2 Magnetoelectric coupling

By combining Neel temperature data from DSC and cooperative displacement data from Rietveld refinement, a linear correlation is found between T_N and (s-t), plotted in figure 44. This relationship has also been reported by others [21, 40], but the backgroud for this is not yet fully understood [21]. However, it is a very interesting observation that opens the possibility for ferroelectric control and stabilization of magnetic ordering, with reference to chapter 1.
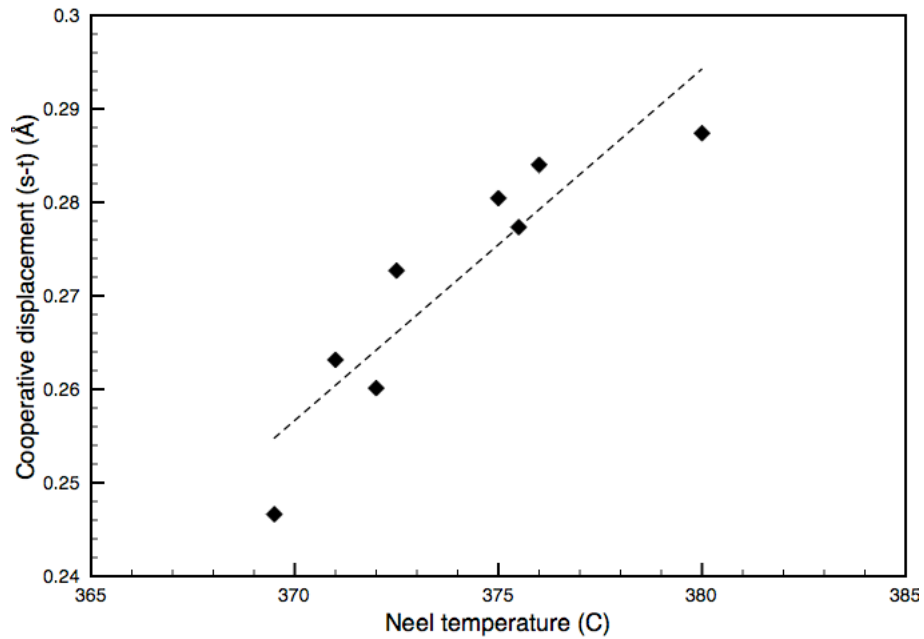
Figure 44: Correlation between Neel temperature and cooperative displacement (s-t), with fitted trendline.

.

6   Conclusions

The aim of work of this project was to investigate specified material properties of $Bi_{0.9}Sm_{0.1}FeO_3$ synthesized by a modified Pechini method and compare the results with relevant litterature to set these results in perspective.

All Pechini syntheses produced the desired perovskite phase, but no product were phase-pure. The most abundant secondary phase is sillenite, but iron rich phases are also present for all syntheses to some extent. The secondary phases decompose at increased calcination temperature, probably due to increased mobility of the ions.

The results from the experiment can be divided in two sections; 1) effects of samarium substitution and 2) finite size effects.

Samarium substitution effetcs   When 10mol% of the bismuth cations is substituted by samarium in $BiFeO_3$ the unti cell geometry is still of the R3c room group, but the tetragonality (c_{norm} / a_{norm}) is lower than for the unsubstituted composition, being 1.015 and 1.010 for $BiFeO_3$ and $Bi_{0.9}Sm_{0.1}FeO_3$ in bulk sizes, respectively. This fact follows the trend of a decrease in tetragonality with decreasing dopant cation radii and/or the dopant concentration, presented by other groups.

Regarding polarization properties, the cooperative displacement of Bi^{3+} and Fe^{3+} cations in $Bi_{0.9}Sm_{0.1}FeO_3$ is lower than for $BiFeO_3$ mainly due to the decrease of lone-pair covalent bonding from bismuth cations. Compared with data from lanthanum substitution, cation size has little or no effect on cooperative displacement. Further, the ferroelectric phase transition temperature T_C decreases upon samarium substitution from 830°C to 459°C for $BiFeO_3$ and $Bi_{0.9}Sm_{0.1}FeO_3$, respectively. This follows the trend of other experiments on substitution by samarium and substitution by other rare-earth cations, that T_C is decreased upon decreasing dopant ionic radii and/or increased dopant concentration.

A prediction of magnetic properties were investigated trough the magnetic phase transition at T_N, which is increased upon 10mol% samarium substitution. This result is in compliance with other reports.

Finite-size effects   There is a clear dependence of crystallite size on the unit cell geometry when sizes below 30nm are approached. The c parameter is then decreasing, in compliance with other reports. However, in these experiments, the a parameter is also decreasing, resulting in a decrease in unit cell volume as an effect of reduced crystallite size, contradictory to results from $BiFeO_3$ for which the unit cell expands. In the case of lanthanum substitution, the a parameter remains constant down to 20nm crystallite sizes. These observations makes an interesting trend for the a parameter size effects as a function of reduced cation radii. The unit cell tetragonality decreases from 1.010 to 1.006 for 30nm and 21nm crystallites, respectively. By extrapolation of the tetragonality trend, the cubic structure (c_{norm} / a_{norm} = 1) is reached slightly below 20nm in crystallite size.

The polarization represented by the cooperative displacement is similarly to unit cell tetragonality decreasing as a function of decreasing crystallite size. However, the decrease in cooperative displacement appears at at larger crystallite sizes, which is probably due to the loss of long-range electrostatic forces in nanocrystallites, and therfore not only an effect of the decreased asymmetry of the unit cell. In this experiments, no ferroelectric phase transition were obtainable from the DSC results of nanocrystallites, but what is believed to be a finite size

effect on T_C is revealed, which is not reported by other groups before. This result comes from the 10-15°C difference in T_C between powders calcined at 850°C and powder that has been quickly heated to 850°C in the DSC intrument. This result was emphasized by a slow-heating DSC run.

The is a clear finite size effect for the magnetic phase transition temperature T_N upon decreasing crystallite size, being 390°C and 369°C for $Bi_{0.9}Sm_{0.1}FeO_3$ in bulk sizes and nanoparticles, respectively. A correlation between cooperative displacement and T_N has also been presented here, prediction a magnetoelectric coupling, but this is rather an interesting observation and not yet fully understood.

Further work   Further work in this field could be to get more results to accompany the results presented here and to increase the range of crystallite sizes. An effort could also be done in achieving smaller crystallite sizes ($<$20nm) to investigate if finite size effects are as expected in such small crystallites. On the ferroelectric properties, powders could be calcined at temperatures between 600°C and 800°C to search for a ferroelectric phase transition in DSC experiments. For the magnetic properties, magnetic spectroscopy could be used to study the magnetic response and compare with theoretical assumptions. The origin of the conductivity of sintered pellets should be addressed for further electrical measurements. Scanning electron microscopy is an applicable tool in this respect.

Material properties at elevated temperatures should be done to investigate the thermodynamics of samarium substituted bismuth ferrite and compared with observations for the pure compound, High-temperature XRD may be used for this. Other characterization methods could also have been used, such as high resolution transmission electron microscopy to study the material at an atomic level.

References

[1] S. M. Selbach. *Structure, stability and phase transitions of multiferroic BiFeO₃*. Doctoral thesis, NTNU (2009).

[2] O. Hatling. *Multiferroic, magnetoelectric nanoparticles: Lanthanum-substituted bismuth ferrite*. Master thesis, NTNU (2011).

[3] D. H. Haneberg. *Samarium-substituted Bismuth Ferrite Piezoelectric Materials*. Project work, NTNU (2010).

[4] David W. Richerson. *Modern Ceramic Engineering*. Taylor & Francis Group (2006).

[5] Charles Kittel. *Introduction to Solid State Physics*. John Wiley & Sons, Inc (2005).

[6] G. Schneider. *Influence of Electric Field and Mechanical Stresses on the Fracture of Ferroelectrics*. Annu. Rev. Mater. Res., 37, 491-538 (2007).

[7] S. Elliot. *The Physics and Chemistry of Solids*. John Wiley & Sons (1998).

[8] R. Ramesh, S. Aggarwal and O. Auciello. *Science and technology of ferroelectric films and heterostructures for non-volatile ferroelectric memories*. Mate. Sci. Eng., 32, 191-236 (2001).

[9] J. F. Scott. *Applications of modern ferroelectrics*. Science, 315, 954-959 (2007).

[10] M. Fiebig. *Revival of the magnetoelectric effect*. J. Phys. D: Appl. Phys., 38, R123-R152 (2005).

[11] J. Rödel, W. J. Klaus, T. P. Seifert, E.-M. Anton, T. Granzow and D. Damjanovic. *Perspective on the Development of Lead-free Piezoceramics*. J. Am. Ceram. Soc., 92 [6], 1153-1177 (2009).

[12] EU-directive 2002/95/EC: *Restriction of the Use of Certain Hazardous Substances in Electrical and Electronic Equipment (RoHS)*. Off. J. Eur. Union, 46 [L37] 19-23 (2003).

[13] EU-directive 2002/96/EC: *Waste electrical and Electronic Equipment (WEEE)*. Off. J. Eur. Union, 46 [L37] 24-38 (2003).

[14] M. Bibes and A. Barthelemy. *Multiferroics: Towards a magnetoelectric memory*. Nat. Mater., 7, 425-426 (2008)

[15] G. Catalan, J. F. Scott. *Physics and Applications of Bismuth Ferrite*. Adv. Mater., 21, 2463-2485 (2009).

[16] J. Wang, J. B. Neaton, H. Zheng, V. Nagarajan, S. B. Ogale, B. Liu, D. Viehland, V. Vaithyanathan, D. G. Schlom, U. V. Waghmare, N. A. Spaldin, K. M. Rabe, M. Wuttig and R. Ramesh. *Epitaxial BiFeO₃ multiferroic thin film heterostructures*. Science, 299, 1719-1722 (2003).

[17] S. Lee, W. Ratcliff, S. W. Cheong and V. Kiryukhin. *Electric field control of the magnetic state in BiFeO₃ single crystals*. Appl. Phys. Lett., 92, 122906 (2008).

[18] C. Ederer and N. A. Spaldin. *Weak ferromagnetism and magnetoelectric coupling in bismuth ferrite.* Phys. Rev. B., 71, 060401(R) (2005).

[19] S. Karimi, I. M. Reaney, Y. Han, J. Pokorny and I. Sterianou. *Crystal chemistry and domain structure of rare-earth doped $BiFeO_3$ ceramics.* J. Mater. Sci., 44, 5102-5112 (2009).

[20] S. Fujino, M. Murakami, V. Anbusathaiah, S.-H. Lim, V. Nagarajan, C. J. Fennie, M. Wuttig, L. Salamanca-Riba and I. Takeuchi. *Combinatorial discovery of a lead-free morphotropic phase boundary in a thin-film piezoelectric perovskite.* Appl. Phys. Lett., 92, 202904 (2008).

[21] S. M. Selbach, T. Tybell, M.-A. Einarsrud and T. Grande. *Size-Dependent Properties of Multiferroic $BiFeO_3$ Nanoparticles.* Chem. Matter, 19, 6478-6484 (2007).

[22] S. M. Selbach, M.-A. Einarsrud and T. Grande. On the Thermodynamic Stability of $BiFeO_3$. Chem. Mater., 21 [1], 169-173 (2009).

[23] J. Tichy, J. Erhart, E. Kittinger and J. Privratska. *Fundamentals of Piezoelectric Sensorics.* Springer-Verlag Berlin Heidelberg (2010).

[24] L. Pardo and J. Ricote. *Multifunctional Polycrystalline Ferroelectric Materials, Processing and Properties.* Springer (2011).

[25] A. L. Kholkin, N. A. Pertsev and A. V. Goltsev. *Piezoelectricity and Crystal Symmetry.* Springer Science (2008).

[26] S. Chattopadhyay, S. D. Kelly, V. R. Palkar, L. Fan and C. U. Segre. *Investigation of Size Effects in Magnetoelectric $BiFeO_3$.* Phys. Scr., Vol T115, 709-713 (2005).

[27] W. Eerenstein, N. D. Mathur and J. F. Scott. *Multiferroic and magnetoelectric materials.* Nature, Vol 442 (2006).

[28] S. C. Abrahams, S. K. Kurtz and P. B. Jamieson. *Atomic Displacement Relationship to Curie Temperature and Spontaneous Polarization in Displacive Ferroelectrics.* Phys. Rev., 172, 551 (1968).

[29] Y. Hu, L. Fei, Y. Zhang, J. Yuan, Y. Wang and H. Gu. *Synthesis of Bismuth Ferrite Nanoparticles via a Wet Chemical Route at Low Temperature.* Journ. Nanomat.,, 797639 (2011).

[30] S. Ghosh, S. Dasgupta, A. Sen and H. S. Maiti. *Low-Temperature Synthesis of Nanosized Bismuth Ferrite by Soft Chemical Route.* Journal of the American Ceramic Society, Vol. 88, Issue 5 (2005).

[31] G. Sushmita, D. Subrata, S. Amarnath and S. M. Himadri. Low-Temperature Synthesis of Nanosized Bismuth Ferrite by Soft Chemical Route. J. Am. Ceram. Soc., 88 [5], 1349-1352 (2005).

[32] J. Wei and D. Xue. *Low-Temperature synthesis of $BiFeO_3$ nanoparticles by ethylenediaminetetraacetic acid complexing sol-gel process.* Mat. Res. Bull., Vol. 43, 12, 3368-3373 (2008).

[33] T.-J. Park, G. C. Papaefthymiou, A. J. Viescas, A. R. Moodenbaugh and S. S. Wong. *Size-Dependent Magnetic Properties of Single-Crystalline Multiferroic BiFeO₃ Nanoparticles.* Nano. Lett., pp 766-772, 7(3) (2007).

[34] P. Fischer, M. Polomska, I. Sosnowska and M. Szymanski. *Temperature dependence of the crystal and magnetic structures of BiFeO₃.* J. Phys. C: Solid St. Phys., 13, 1931-1940 (1980)

[35] M.P. Pechini, US Patent 3, 330, 697 (July 11, 1967).

[36] L. S. Birks and H. Friedman. *Particle size determination from x-ray line broadening.* J. Appl. Phys., 17, 687-692 (1946).

[37] R. Palai, R. S. Katiyar, H. Schmid, P. Tissot, S. J. Clark, J. Robertson, S. A. T. Redfern, G. Catalan and J. F. Scott. *β phase and γ-β metal-insulator transition in multiferroic BiFeO3.* Phys. Rev. B., 77, 014110 (2008).

[38] K. S. Nalwa and A. Garg. *Phase evolution, magnetic and electrical properties in Sm-doped bisumth ferrite.* Jour. Appl. Phys., 103, 044101 (2008).

[39] R. D. Shannon. *Revised Effective Ionic-Radii and Systematic Studies of Interatomic Distances in Halides and Chalcogenides.* Acta Crystallogr. Sec. A, 32 751–767 (1976).

[40] T. Zhao, A. Scholl, F. Zavaliche, K. Lee, M. Barry, A. Doran, M. P. Cruz, Y. H. Chu, C. Ederer, N. A. Spaldin, R. R. Das, D. M. Kim, S. H. Baek, C. B. Eom and R. Ramesh. *Electrical control of antiferromagnetic domains in multiferroic BiFeO₃ films at room temperature.* Nat. Matter., 5, 823-829 (2006).

[41] D. Lebeugle, D. Colson, A. Forget, M. Viret, A. M. Bataille and A. Gukasov. *Electric-field-induced spin flop in BiFeO₃ single crystals at room temperature.* Phys. Rev. Lett., 100, 227602 (2008).

[42] P. Rovillain, M. Cazayous, Y. Gallais, A. Sacuto, R. P. S. M Lobo, D. Lebeugle and D. Colson. *Polar phonons and spin exitations coupling in multiferroic BiFeO₃ crystals.* Phys. Rev. B, 79, 180411(R) (2009).

[43] Q. M. Zhang, W. Y. Pan, S. J. Jang, L. E. Cross. *Domain wall exitations and their contributions to the weak-signal response of doped lead zirconate titanate ceramics.* J. Appl. Phys., 64, 6445-6451 (1988).

[44] I. M. Reaney. *Octahedral tilting, domain structure and piezoelectricity in perovskites and related ceramics.* J. Electroceram, 19, 1-8 (2007).

[45] S. Shetty, V. R. Palkar and R. Pinto. *Size effect study in magnetoelectric BiFeO₃ system.* Pramana Jour. Phys., 58, 1027-1030 (2002).

[46] C.-J. Cheng, D. Kan, S.-H. Lim, W. R. McKenzie, P. R. Munroe, L. G. Salamanca-Riba, R. L. Withers, I. Takeuchi and V. Nagarajan. *Structural transitions and complex domain structures across a ferroelectric-to-antiferroelectric phase boundary in epitaxial Sm-doped BiFeO₃ thin film.* Phys. Rev., B 80 014109 (2009).

[47] V. V. Shvartsman, W. Kleeman, R. Haumont and J. Kreisel. *Large bulk polarization and regular domain structure in ceramic $BiFeO_3$.* Appl. Phys. Lett., 90, 172115 (2007).

[48] Y. H. Chu, L. W. Martin, M. B. Holcomb, M. Gajek, S. J. Han, Q. He, N. Balke, C. H. Yang, D. Lee, W. Hu, Q. Zhan, P. L. Yang, A. Fraile-Rodriguez, A. Scholl, S. X. Wang and R. Ramesh. *Electric-field control of local ferromagnetism using a magnetoelectric multiferroic.* Nat. Mater., 7, 478-482 (2008).

[49] P. Ravindran, R. Vidya, A. Kjekshus, H. Fjellvåg and O. Eriksson. *Theoretical investigation of magnetoelectric behavior in $BiFeO_3$.* Phys. Rev. B, 74, 224412 (2006).

[50] J. B. Goodenough. *Electronic and ionic transport properties and other physical aspects of perovskites.* Rep. Prog. Phys., 67, 1915-1993 (2004).

[51] V. M. Goldschmidt. *Naturwissenschaften.* 14, 477 (1926).

[52] D. H. Loyd. *Physics Laboratory manual.* Thomson Brooks/Cole (2002).

[53] H. M. Rietveld. *A Profile Refinement Method for Nuclear and Magnetic Structures.* Jour. Appl. Crystallogr., 2, 65 (1969).

[54] G. W. H. Höhne, W. F. Hemminger and H.-J. Flammersheim. *Differential Scanning Calorimetry.* Springer-Verlag (2003).

[55] H. Uchida, R. Ueno, H. Funakubo and S. Koda. *Crystal structure and ferroelectric properties of rare-earth substituted $BiFeO_3$ thin films.* Jour. Appl. Phys., 100, 014106 (2006).

[56] Q.-H. Jiang, C.-W. Nan, Y. Wang, Y.-H. Liu and Z.-J. Shen. *Synthesis and properties of multiferroic $BiFeO_3$ ceramics.* J. Electroceram, 21, 690-693 (2008).

[57] H. Yang, T. Xian, Z. Q. Wei, J. F. Dai, J. L. Jiang and W. J. Feng. *Size-controlled synthesis of $BiFeO_3$ nanoparticles by a soft-chemistry route.* J. Sol-Gel Sci. Technol., 58, 238-243 (2011).

[58] S. Karimi, I. M. Reaney, I. Levin and I. Sterianou. *Nd-doped BiFeO3 ceramics with antipolar order.* Appl. Phys. Lett., 94, 112903 (2009).

[59] V. A. Khomchenko, J. A. Paixão, B. F. O. Costa, D. V. Karpinsky, A. L. Kholkin, I. O. Troyanchuk, V. V. Shvartsman, P. Borisov, and W. Kleemann. *Structural, ferroelectric and magnetic properties of $Bi_{0.85}Sm_{0.15}FeO_3$ perovskite.* Cryst. Res. Technol. 46 (3), 238 – 242 (2011).

[60] G. L. Yuan, S. W. Or, J. M. Liu, and Z. G. Liu. *Structural transformation and ferroelectromagnetic behavior in single-phase $Bi_{1-x}Nd_xFeO_3$ multiferroic ceramics.* Appl. Phys. Lett. 89, 052905 (2006).

[61] J. R. Sahu and C.N.R. Rao. *Beneficial modification of the properties of multiferroic BiFeO3 by cation substitution.* Solid St. Sci., 9, 950-954 (2007).

[62] D. Lebeugle, D. Colson, A. Forget, M. Viret, P. Bonville, J.F. Marucco, S. Fusil. *Room-temperature coexistence of large electric polarization and magnetic order in $BiFeO_3$ single crystals.* Phys. Rev. B 76, 024116 (2007).
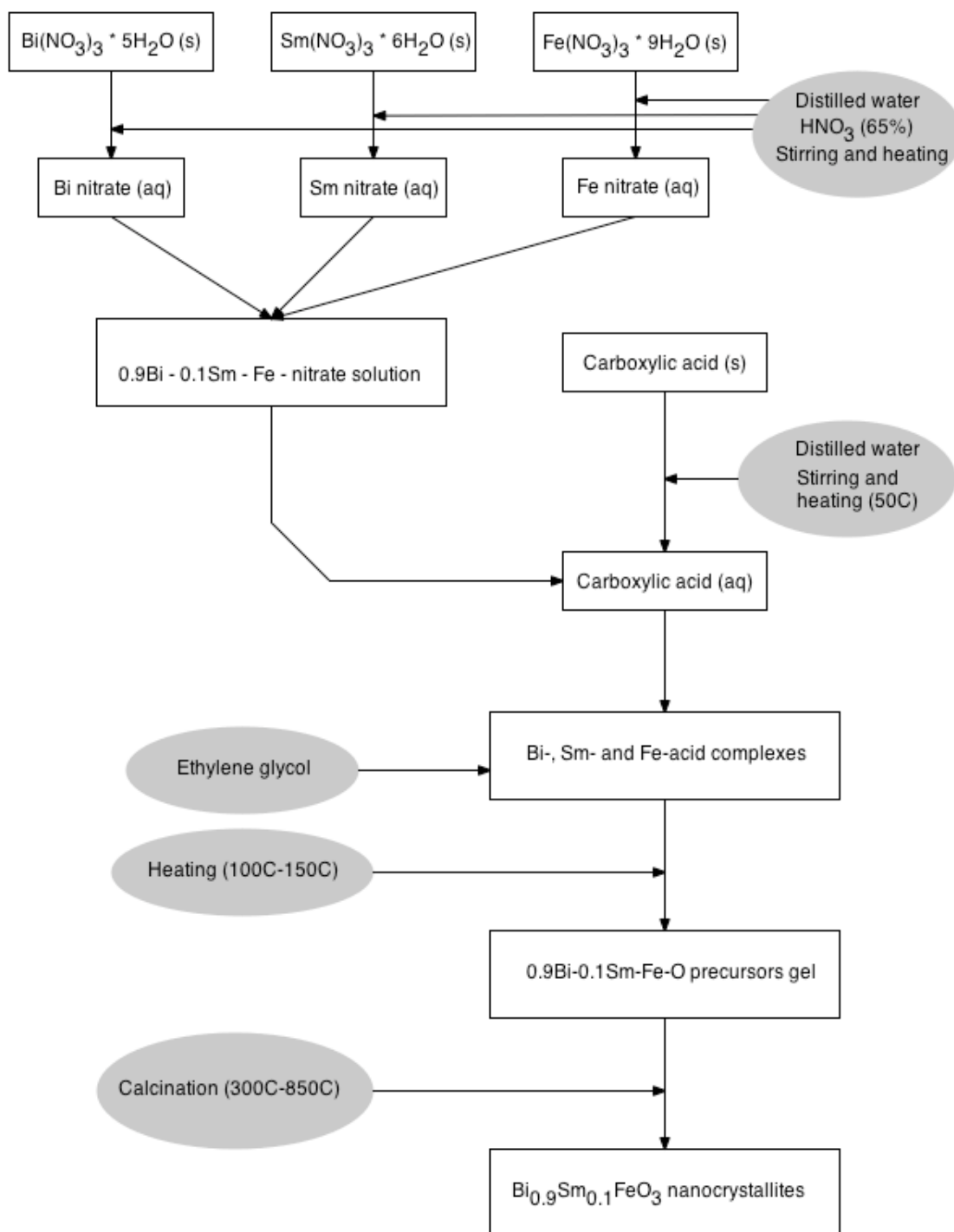
Appendix A - Synthesis scheme

Figure 45: Synthesis scheme for modified Pechini synthesis of $Bi_{0.9}Sm_{0.1}FeO_3$.

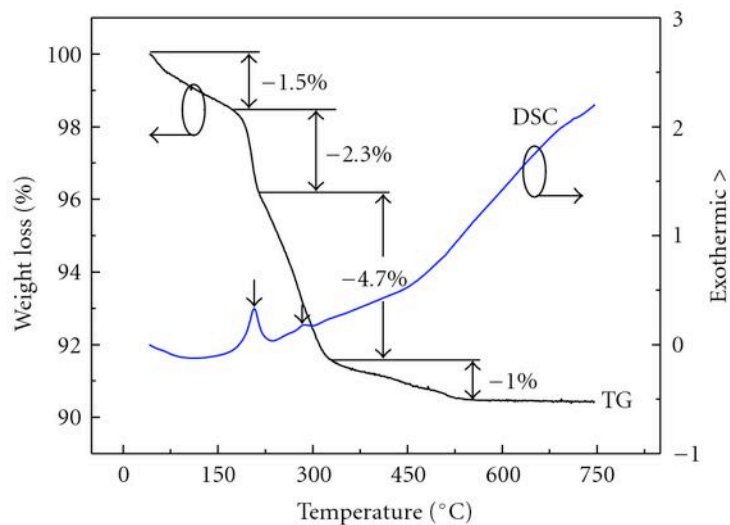# Appendix B - Choice of carboxylic acid in synthesis

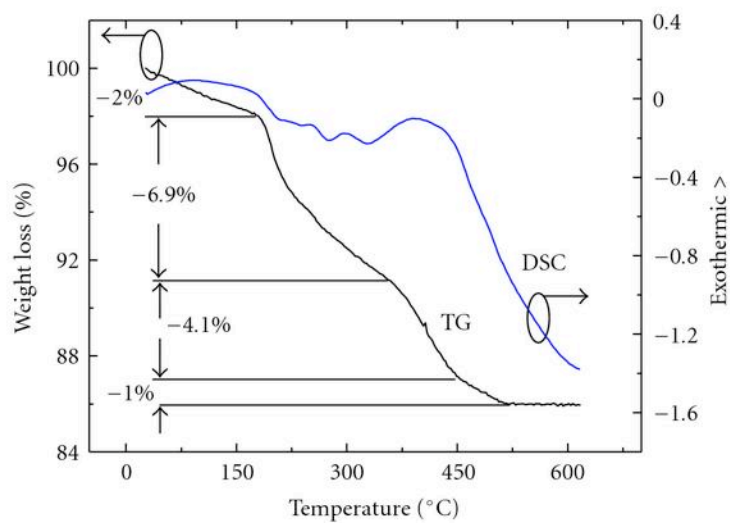Figure 46: TG and DSC curves for calcination of BiFeO$_3$ sol-gel product with citric acid [29].

Figure 47: TG and DSC curves for calcination of BiFeO$_3$ sol-gel product with tartaric acid [29].
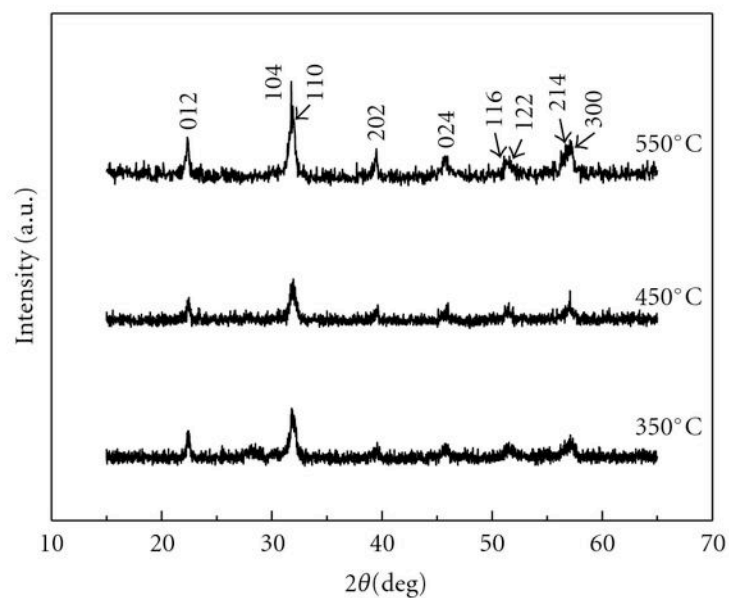
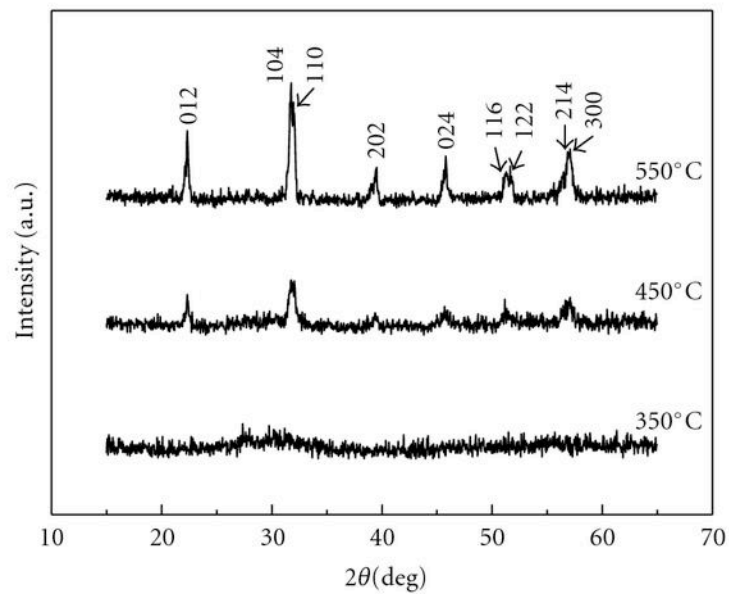Figure 48: XRD diffractograms for calcined BiFeO$_3$ sol-gel synthesized powder using citric acid [29].

Figure 49: XRD diffractograms for calcined BiFeO$_3$ sol-gel synthesized powder using tartaric acid [29].

Appendix C - Overview of syntheses used for experiments

Synt. #	[Total cation]	Carb. acid	[carb. acid]	pH	EG	Hot plate	Usage / Comments
3	0.2 M	Tartaric	0.2 M	~ 2	Yes	130°C	• Sintered pellets • Low-quality XRD
4	0.2 M	Citric	0.2 M	~ 2	Yes	130°C	• Citric acid testing to achieve smaller crystallites • Low-quality XRD
12	0.2 M	Tartaric	0.3 M	0-1	Yes	130°C	• High-quality XRD • Rietveld refinement • All DSC runs
16	0.2 M	Tartaric	0.2 M	0-1	No	130°C	• Test synthesis with 25mol% less bismuth precursor • Low-quality XRD

Table 6: Overview of relevant syntheses

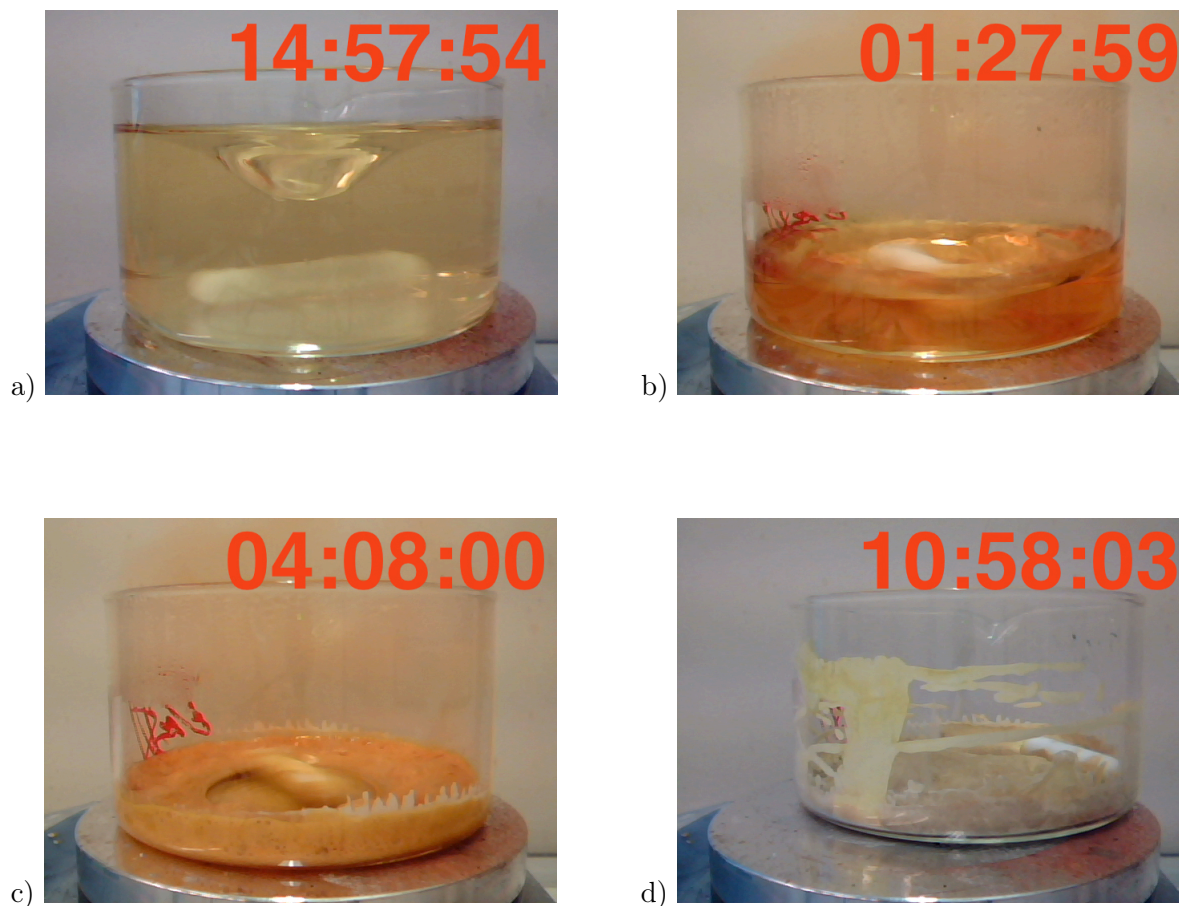## Appendix D - Photographs

Figure 50: Photographs taken of synthesis 3 during the synthesis process. Actual time is inserted in red (first picture is day 1, the other are day 2). a) Initial solution of precursor solution, diluted carboxylic acid and ethylene glycol. b) Evaporation of solvent (DI-water). c) Gel formation. d) Finished dry product. Note the jar has been moved by the magnet when the product was solidified.
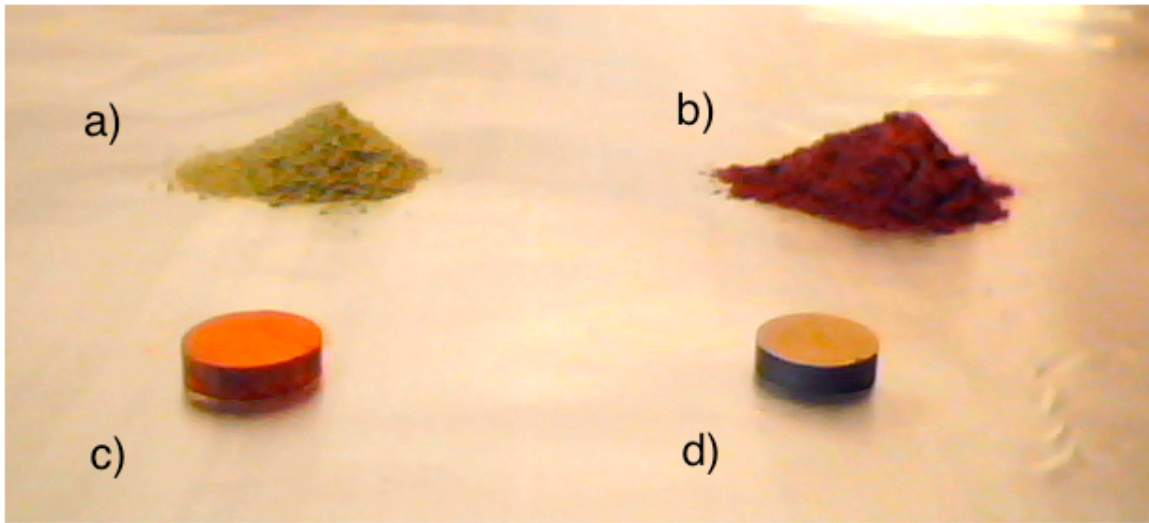
Figure 51: Photographs of sample materials. a) Uncalcined grained powder. b) Calcined powder. c) Green body pellet d) Sintered pellet with gold electrodes.

Appendix E - Pellet density approximation

The caliper and wieght method used to estimate the relative density of sintered pellets use the assumption that the pellet geometry is a perfect cylinder with diameter Ø and height t, illustrated in figure 52. The volume V of the pellet can then be estimated:

$$V = \pi t \left(\frac{\emptyset}{2}\right)^2$$

The mass density ρ of the m,aterial the pellet is made from is then used to calculate what the mass of the pellet would have been if it was 100% dense:

$$m_{dense} = \rho V$$

The actual mass of the pellet is weighted and divided by m_{dense} to calculate the relative density:

$$\text{Relative density } (\%) = 100 \cdot \frac{m_{actual}}{m_{dense}}$$

Figure 52: Pellet geometry represented as a perfect cylinder with diameter Ø and height t.